

# Practical Predictability of the 20 May 2013 Tornadic Thunderstorm Event in Oklahoma: Sensitivity to Synoptic Timing and Topographical Influence

YUNJI ZHANG

*Laboratory for Climate and Ocean–Atmosphere Studies, Department of Atmospheric and Oceanic Sciences, School of Physics, Peking University, Beijing, China, and Department of Meteorology, The Pennsylvania State University, University Park, Pennsylvania*

FUQING ZHANG AND DAVID J. STENSRUD

*Department of Meteorology, The Pennsylvania State University, University Park, Pennsylvania*

ZHIYONG MENG

*Laboratory for Climate and Ocean–Atmosphere Studies, Department of Atmospheric and Oceanic Sciences, School of Physics, Peking University, Beijing, China*

(Manuscript received 27 November 2014, in final form 16 March 2015)

## ABSTRACT

The practical predictability of severe convective thunderstorms during the 20 May 2013 severe weather event that produced the catastrophic enhanced Fujita scale 5 (EF-5) tornado in Moore, Oklahoma, was explored using ensembles of convective-permitting model simulations. The sensitivity of initiation and the subsequent organization and intensity of the thunderstorms to small yet realistic uncertainties in boundary layer and topographical influence within a few hours preceding the thunderstorm event was examined. It was found that small shifts in either simulation time or terrain configuration led to considerable differences in the atmospheric conditions within the boundary layer. Small shifts in simulation time led to changes in low-level moisture and instability, primarily through the vertical distribution of moisture within the boundary layer due to vertical mixing during the diurnal cycle as well as advection by low-level jets, thereby influencing convection initiation. Small shifts in terrain led to changes in the wind field, low-level vertical wind shear, and storm-relative environmental helicity, altering locally enhanced convergence that may trigger convection. After initiation, an upscale growth of errors resulting from deep moist convection led to large forecast uncertainties in the timing, intensity, structure, and organization of the developing mesoscale convective system and its embedded supercells.

## 1. Introduction

The tornado outbreak during 18–21 May 2013 that affected parts of the Midwest and Great Plains was one of the most disastrous tornado outbreaks in recent years. The tornado that struck Moore, Oklahoma, and adjacent regions on the afternoon of 20 May 2013 was estimated to be enhanced Fujita scale 5 (EF-5), the strongest of this year and the first EF-5 tornado since the 22 May 2011

Joplin, Missouri, tornado, and resulted in catastrophic casualties and damages [an overview of this tornado and accompanying synoptic conditions will be provided in [section 2](#); see also [Atkins et al. \(2014\)](#), [Burgess et al. \(2014\)](#), and [Gravelle et al. \(2015\)](#)]. A high probability of tornado occurrence was shown in the day-1 convective outlook issued earlier that day by the Storm Prediction Center (SPC), and the numerous severe convective storms observed in Texas, Oklahoma, Kansas, and Missouri were also qualitatively predicted more than 12 h in advance by the Rapid Refresh (RAP) model and the High-Resolution Rapid Refresh (HRRR) model that were both initialized from a RAP analysis valid at 0600 UTC of this day (LST = UTC – 0500; UTC will be used hereafter). However, when the location and development of single

---

*Corresponding author address:* Zhiyong Meng, Laboratory for Climate and Ocean–Atmosphere Studies, Department of Atmospheric and Oceanic Sciences, School of Physics, Peking University, 209 Chengfu Rd., Haidian District, Beijing 100871, China.  
E-mail: zymeng@pku.edu.cn

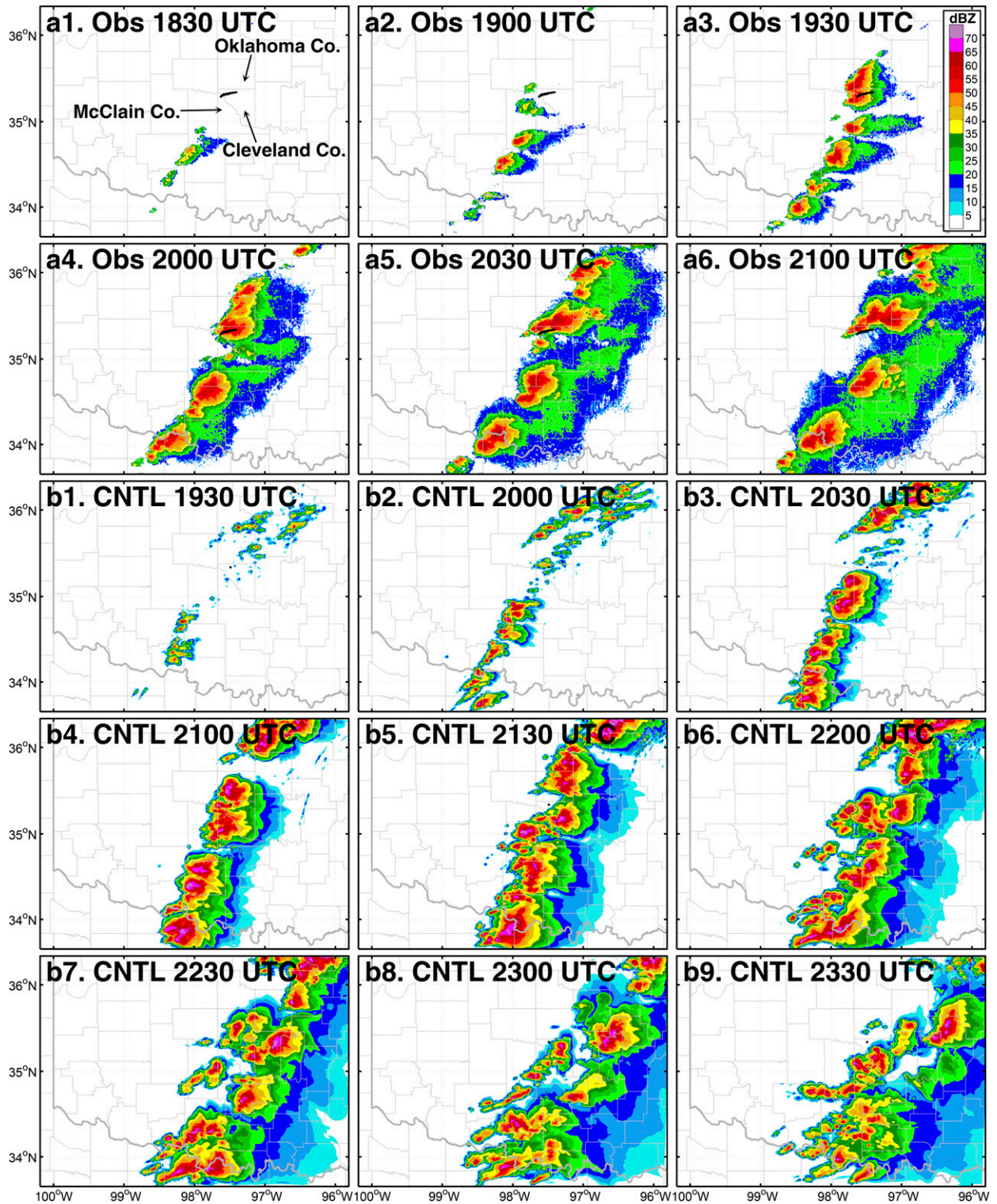


FIG. 1. Composite reflectivity of (a) observations that mapped using KTLX and KFDR radars from 1830 to 2100 UTC every 30 min, and (b) CNTL and (c) CNTL\_15Z simulations from 1930 to 2330 UTC every 30 min. (a1) County names mentioned in the text are indicated. The thick line in the northwest corner of Cleveland County in (a) indicates the track of the tornado.

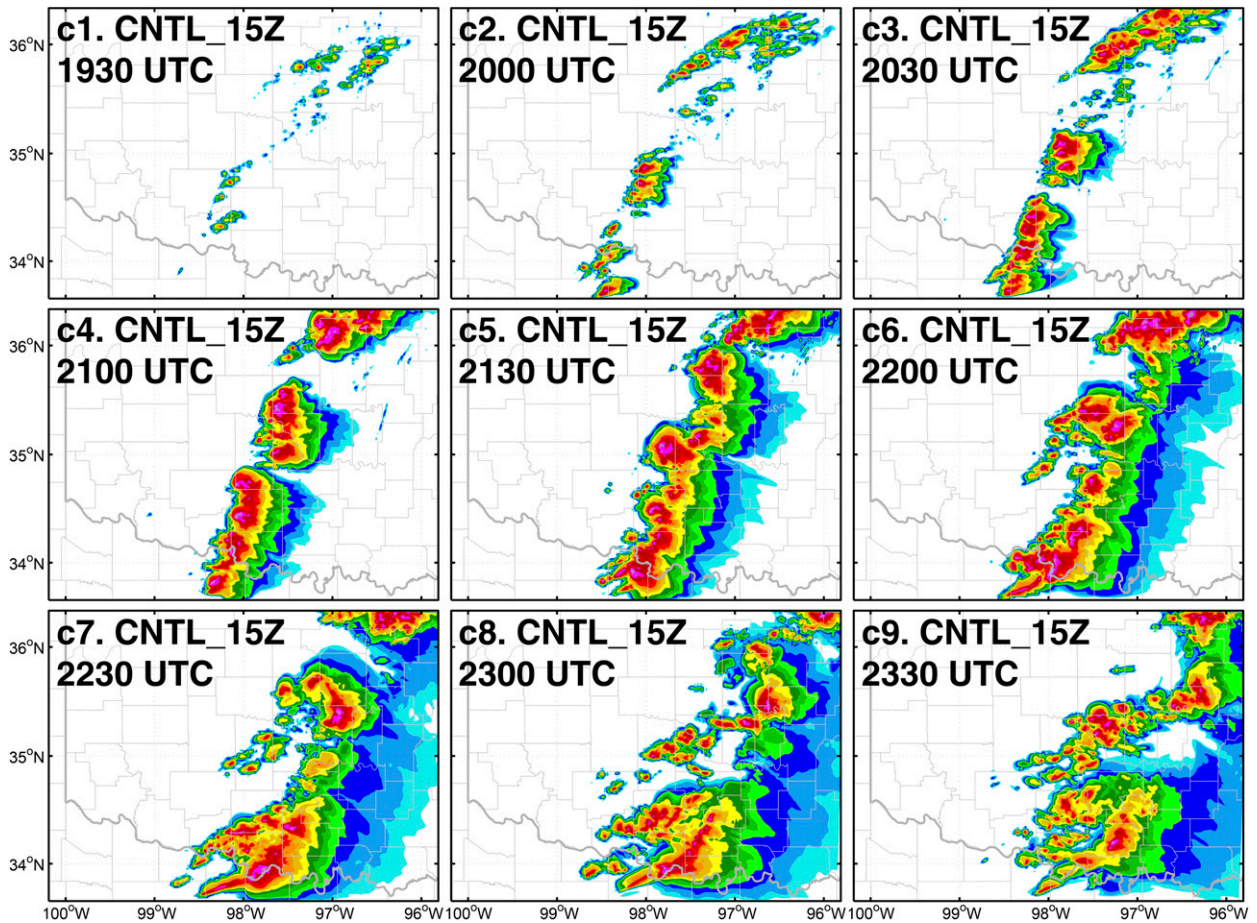


FIG. 1. (Continued)

convective storms were inspected closely, it is clear that numerically simulated storms in both these models contained errors when comparing against their observed counterparts. These errors in model predictions revealed the currently unavoidable limitations of practical predictability.

The concept of practical predictability was first proposed in Lorenz (1982). Different from the intrinsic predictability (Lorenz 1963, 1969) that is defined as the “extent to which prediction is possible if an optimum procedure is used” (Lorenz 1996), practical predictability refers to “the extent to which we ourselves are able to predict by the best-known procedure, either currently or in foreseeable future” (Lorenz 1996). Furthermore, practical predictability is necessarily a moving target; as the practical error continues to be reduced while the prediction procedure is approaching an optimum, the limit of practical predictability would eventually approximate the limit of intrinsic predictability. As indicated by its definition, practical predictability is limited by

realistic uncertainties existing in the present forecast models and their initial conditions. The procedures of data assimilation, the adequacy of observations that are ingested during data assimilation, and deficiencies in the numerical models may all contribute to these uncertainties.

Most works on practical predictability of mesoscale weather phenomena have been focused on relatively larger systems such as snowstorms (e.g., Zhang et al. 2002), tropical cyclones (e.g., Sippel and Zhang 2008; Zhang et al. 2014), and MCSs (e.g., Zhang et al. 2006; Melhauser and Zhang 2012; Wu et al. 2013; Wandishin et al. 2008, 2010). Results showed that forecasts could be very sensitive to initial and model uncertainties. Huge forecast differences may be observed when physical parameterization schemes of cumulus, microphysics, and PBL processes were varied (Zhang et al. 2006; Wu et al. 2013). Forecast errors induced by realistic initial uncertainties could be bigger than those induced by decreasing model resolution (Bei and Zhang 2007). By halving initial error magnitude, the percentage of

ensemble members that successfully produced identifiable MCSs (“success rate” of MCSs) could be increased from 70% to nearly 85% (Wandishin et al. 2008, 2010). It was found that the quality of initial moisture is very important for subsequent forecasts (Wu et al. 2013). Model resolution and accompanying parameterization schemes might further influence the moist convective processes (Sippel and Zhang 2008; Wu et al. 2013).

Studies focusing on the practical predictability of severe thunderstorms were comparably rare. Focusing on the 3 May 1999 southern plains tornado outbreak, Roebber et al. (2002) found that in a weakly forced environment, forecast errors in synoptic conditions could regulate the initiation and organization mode of convections. Recently, an idealized study on the practical predictability of supercell thunderstorm evolution was presented in Cintineo and Stensrud (2013). The success rate of supercells was gradually decreased with the increase of forecast lead times as expected. Practical predictability of supercell features also generally decreased when the size of these features became smaller in scale, and areal extent of cold pools was extremely difficult to predict accurately.

However, as pointed out in Cintineo and Stensrud (2013), one of the limitations of their work was their utilization of horizontally homogeneous environments. On the other hand, although Roebber et al. (2002) examined a real atmospheric weather event in the storm scales, to what extent the impact of synoptic regulation could have and how the influence takes place has not been well documented so far. To help fill this knowledge gap, this study was based on the severe thunderstorm event in Oklahoma on 20 May 2013 using a convective-permitting numerical model, and was primarily focused on two different sources of error that could limit practical predictability of thunderstorms in current severe thunderstorm predictions. One of the errors considered here is a delay or advance of synoptic conditions in global model forecasts, which may influence regional simulations when initialized using these temporally shifted global models; the other is incorrect locations of initiated convections in numerical models due to errors in initial conditions or/and numerical models, which may influence later development and organizational mode of the simulated storms.

This paper is organized as follows. The tornado, its parent thunderstorm, and associated synoptic conditions are briefly discussed in section 2. Section 3 introduces the numerical model and its performance in simulating this event. The impact of synoptic timing and topographical influence are presented in sections 4 and 5, respectively, and section 6 is a summary.

## 2. Overview of the 20 May 2013 Moore, Oklahoma, tornadic thunderstorm event

The tornado that struck central Oklahoma during the local early afternoon of 20 May 2013 was one of the most disastrous tornadoes in the United States of that year. The tornado touched down at the northern tip of McClain County, Oklahoma, at 1956 UTC and moved eastward into Cleveland County, Oklahoma (county locations and tornado track are shown in Fig. 1a1). The NWS in Norman, Oklahoma, issued a tornado warning for adjacent areas at 1940 UTC, 16 min before the tornado touched down, and issued a tornado emergency for northwestern McClain County, southern Oklahoma County, and northern Cleveland County at 2001 UTC. Before the tornado lifted at 2035 UTC, 39 min after touching down, it laid down a path of destruction 23.25 km in length and 1.74 km in maximum width across a populated area of Moore, Oklahoma, and hit two elementary schools, a high school, and a hospital. The damage survey team determined that the tornado produced EF-5 damage, suggesting peak winds of  $94 \text{ m s}^{-1}$  ( $340 \text{ km h}^{-1}$ ). This tornado caused 24 direct fatalities, hundreds of injuries, and an estimated property damage of \$2 billion. It was the deadliest tornado in the United States since the Joplin, Missouri, tornado on 22 May 2011, and the third costliest tornado in U.S. history [information available at <http://www.srh.noaa.gov/oun/?n=events-20130520>; detailed damage analysis can be found in Atkins et al. (2014) and Burgess et al. (2014)].

The synoptic conditions on 20 May combined to produce ingredients known to be conducive to severe weather (Johns and Doswell 1992; McNulty 1995; Stensrud et al. 2003; Uccellini 2014). The 1200 UTC upper-air analyses from the SPC showed a cutoff low at 500 hPa centered over South Dakota with southwesterly flow across the southern plains. An upper-level shortwave trough was moving eastward over New Mexico with 300-hPa wind speeds exceeding  $75 \text{ m s}^{-1}$ . At the surface, a cold front extended southward from the surface low in South Dakota, crossing eastern Kansas and western Oklahoma. A strong low-level jet was present ahead of the cold front and advected moisture northward toward the frontal region, helping to support morning values of CAPE above  $2000 \text{ J kg}^{-1}$  in central Oklahoma.

By 1800 UTC, the upper-level shortwave trough had moved over the Oklahoma Panhandle (Fig. 2a) and a weak surface low had developed in northwestern Texas and southwestern Oklahoma (Fig. 2c). Near the surface, warm and moist southerly flow from the Gulf of Mexico had created a warm tongue superimposed on the surface low (Fig. 2c) and a meridionally oriented dryline, a feature long recognized as a boundary that could trigger deep

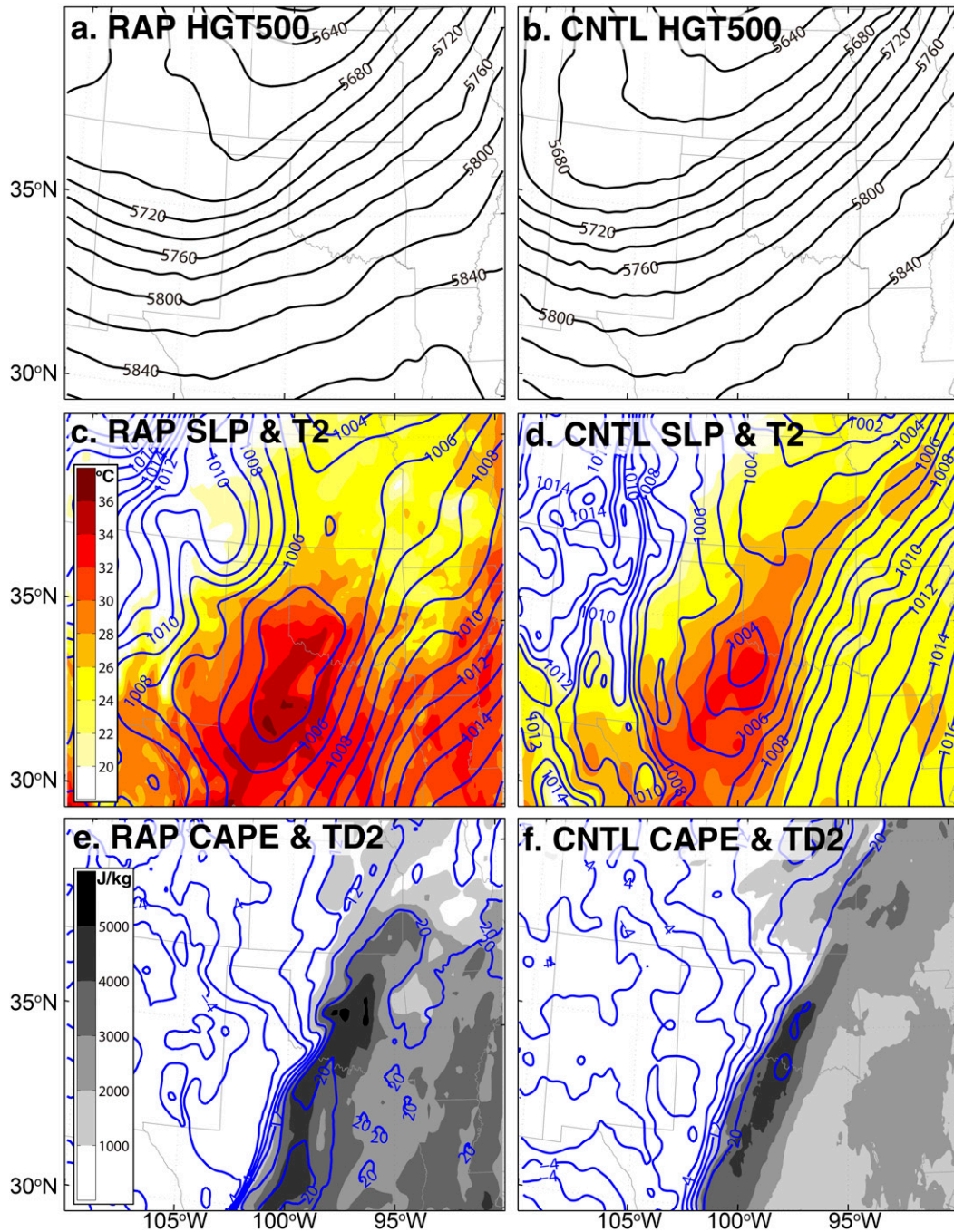


FIG. 2. Synoptic conditions at 1800 UTC 20 May 2013 of (a),(b) 500-hPa geopotential height (every 20 m); (c),(d) sea level pressure (blue, every 1 hPa) and surface 2-m temperature (shaded;  $^{\circ}\text{C}$ ); and (e),(f) 2-m dewpoints (blue, every  $2^{\circ}\text{C}$ ) and surface-based CAPE (shaded;  $\text{J kg}^{-1}$ ). (a),(c),(e) Plotted using RAP analysis and (b),(d),(f) plotted using smoothed D02 fields of the CNTL simulation.

moist convection (Rhea 1966; Bluestein and Parker 1993; Ziegler and Rasmussen 1998), had developed in western Oklahoma and Texas (Fig. 2e). With surface dewpoints above  $20^{\circ}\text{C}$  in central and eastern Oklahoma, the air mass in central and southern Oklahoma was very unstable with

surface-based (SB) CAPE values exceeding  $5000 \text{ J kg}^{-1}$  (Fig. 2e). Severe convective storms were expected under these environmental conditions; the SPC had issued a 10% or greater probability of tornadoes to occur in this region in its day 1 0600 UTC convective outlook.

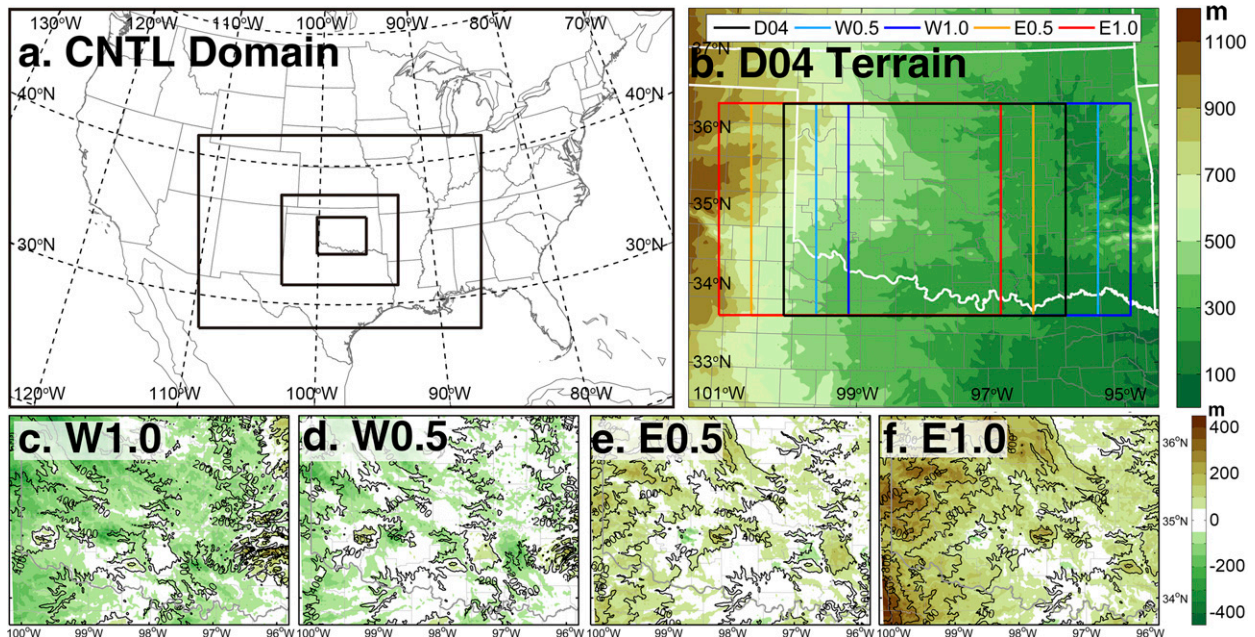


FIG. 3. (a) Model domain configuration, (b) terrain height (shaded; m) in D04 and adjacent regions with rectangles in different colors indicate respective topography that were used in different simulations of TOPO\_SHIFT experiment, and applied model topography (contours every 100 m) and their respective difference (shaded; m) from CNTL (shaded) of (c) W1.0, (d) W0.5, (e) E0.5, and (f) E1.0.

Composite reflectivity (horizontal distribution of vertically maximum radar reflectivity) mapped using base reflectivity from two WSR-88Ds at Fredrick (KFDR) and Twin Lakes (KTLX) in Oklahoma shows that convection initiated first over southern Oklahoma near the border of Texas around 1830 UTC (Fig. 1a1). The convection associated with the Moore tornado appeared around 1900 UTC (Fig. 1a2) and rapidly intensified into a supercell thunderstorm (Fig. 1a3). Less than an hour after initiation of this thunderstorm, a clear signature of rotation could be seen in radar radial velocity fields (not shown). The tornadic thunderstorm tracked eastward across northern Cleveland County and southern Oklahoma City (Figs. 1a4 and 1a5). Several other discrete storms also developed across Oklahoma, forming a southwest–northeast-oriented line of thunderstorms (Fig. 1a6).

### 3. Methodology

#### a. Model configuration

The numerical model utilized in this study was the fully compressible, nonhydrostatic WRF-ARW Model (Skamarock et al. 2008) version 3.5. Four one-way nested domains of  $201 \times 121$ ,  $256 \times 175$ ,  $316 \times 244$ , and  $400 \times 301$  horizontal grid points with 27-, 9-, 3- and 1-km horizontal grid spacing, respectively, were used. The largest domain D01 covered the entire CONUS, while

the innermost domain D04 covered most of Oklahoma (Fig. 3a). There were 61 terrain-following hydrostatic–pressure vertical levels topped at 50 hPa in all domains, with 14 levels located in the lowest 1 km AGL.

Based on the past experiences of the authors and preliminary sensitivity experiments, several physical parameterization schemes were chosen for all the simulations conducted in this study. These schemes included: the Thompson et al. (2008) microphysics scheme, the Grell 3D ensemble cumulus scheme (Grell and Dévényi 2002) that was used only on the 27-km domain D01, the MM5 similarity surface layer scheme (Zhang and Anthes 1982), the RUC land surface model (Benjamin et al. 2004), the Mellor–Yamada–Nakanishi–Nino (MYNN) level-2.5 PBL scheme (Nakanishi and Niino 2009), the RRTM longwave radiation scheme (Mlawer et al. 1997), and the Goddard shortwave radiation scheme (Chou and Suarez 1994). Simulated radar reflectivity was calculated using the built-in module of the Thompson microphysics scheme.

#### b. Experiment design

The control deterministic forecast (CNTL) initialized the four model domains at 1200 UTC 19 May, 1200 UTC 20 May, 1200 UTC 20 May, and 1500 UTC 20 May, respectively, and integrated separately until 0000 UTC 21 May. The initial and lateral boundary conditions (IC and LBC, respectively) of D01 were provided by GFS analysis and subsequent forecast starting at 1200 UTC

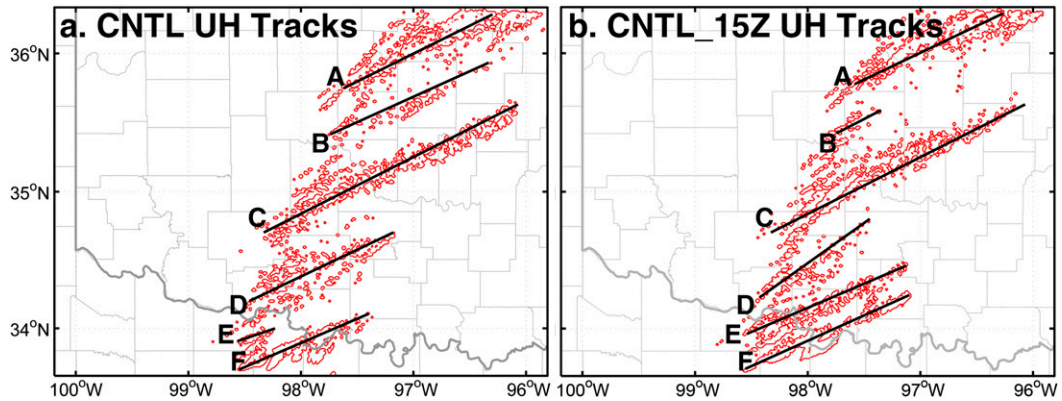


FIG. 4. Contours of  $180 \text{ m}^2 \text{ s}^{-2}$  updraft helicity of (a) CNTL and (b) CNTL\_15Z simulations. The black lines and accompanying letters indicate identified mesocyclone tracks.

19 May; for other inner domains, their ICs and LBCs were provided by simulations of their respective parent domains (i.e., one-way nested).

It is well known that numerical model forecasts often contain errors in the timing, amplitude, and location of synoptic-scale features (Schultz and Doswell 2000; Elmore et al. 2006) and surface mesoscale features (Roebber and Gehring 2000; Colle et al. 2001; Coffey et al. 2013), while model forecasts of boundary layer depth can have absolute mean errors of several hundred meters (Coniglio et al. 2013) and forecasts using different parameterization schemes can often vary by a factor of 2 (Bright and Mullen 2002; Stensrud and Weiss 2002). Location errors of simulated convections in numerical models, especially during the initiation stage of storms, may also lead to errors in topographical influence, as the atmospheric feature would interact with an incorrect representation of the underlying topography. Thus, to account for the impact of synoptic timing and boundary layer depth, as well as topographical influence, two sets of ensemble forecasts were generated. The impact of synoptic timing and boundary layer depth was examined by using an ensemble with only initial differences but exactly the same model configuration, thus all errors in the forecast evolved only from initial conditions while there was no model error. The impact of topography was examined by using exactly the same initial condition and the same numerical model but with a modified topography, thus only model errors associated with underlying surface were introduced while there was no analysis error.

Changes in synoptic timing and boundary layer depth were introduced by simply recentering nine different times from the CNTL simulation to one specific time and using the recentered fields as ICs for a small ensemble. To be specific, all the D03 CNTL output variables every 15 min were averaged between 1400 and 1600 UTC to produce a three-dimensional time-mean CNTL state.

Nine three-dimensional D03 “perturbation” fields were produced by subtracting this time-mean state from the original values of each of the nine 15-min output times. These perturbations were added onto the 1500 UTC model state to produce a nine-member ensemble. The outermost 40 grid points of D03 on all four sides were designed as a “buffer zone” where the ICs of each member were smoothly transitioned to match the 1500 UTC CNTL output by multiplying the perturbations by a linearly decreasing factor from 1 to 0. Thus, all ICs had identical values at the boundaries and the same LBC that was used in CNTL was applied to all of the ensemble members. All atmospheric variables in standard WRF output files, both prognostic and diagnostic ones, were “perturbed” following this manner. All the ensemble members were initialized at 1500 UTC and integrated for 9 h with one-way nested two domains of 3-km D03 and 1-km D04; this ensemble will be referred to as TIME\_SHIFT. Using an additional 3-km domain together with the 1-km D04 could avoid the possible influence of the deterministic LBC; this influence will also be explored in section 4. To construct a perfect-model scenario and account for the impact of cold start of the ensemble at 1500 UTC, an additional simulation initialized from the mean of the ensemble ICs (i.e., the 1500 UTC output of CNTL) for the same simulation time period was also carried out (denoted CNTL\_15Z) as the reference simulation to the TIME\_SHIFT ensemble forecast.

Instead of shifting atmospheric conditions, the terrain was shifted so as to initiate convections in incorrect topographical locations. These changes in topography were created in a manner similar to TIME\_SHIFT, also with both D03 and D04 modified. First, the topography in the 3-km D03 was moved either to the west or to the east by either  $0.5^\circ$  or  $1.0^\circ$  (denoted as W0.5, E0.5, W1.0, and E1.0, respectively) with a same buffer zone of 40 grid points. The topography in 1-km D04 was moved in

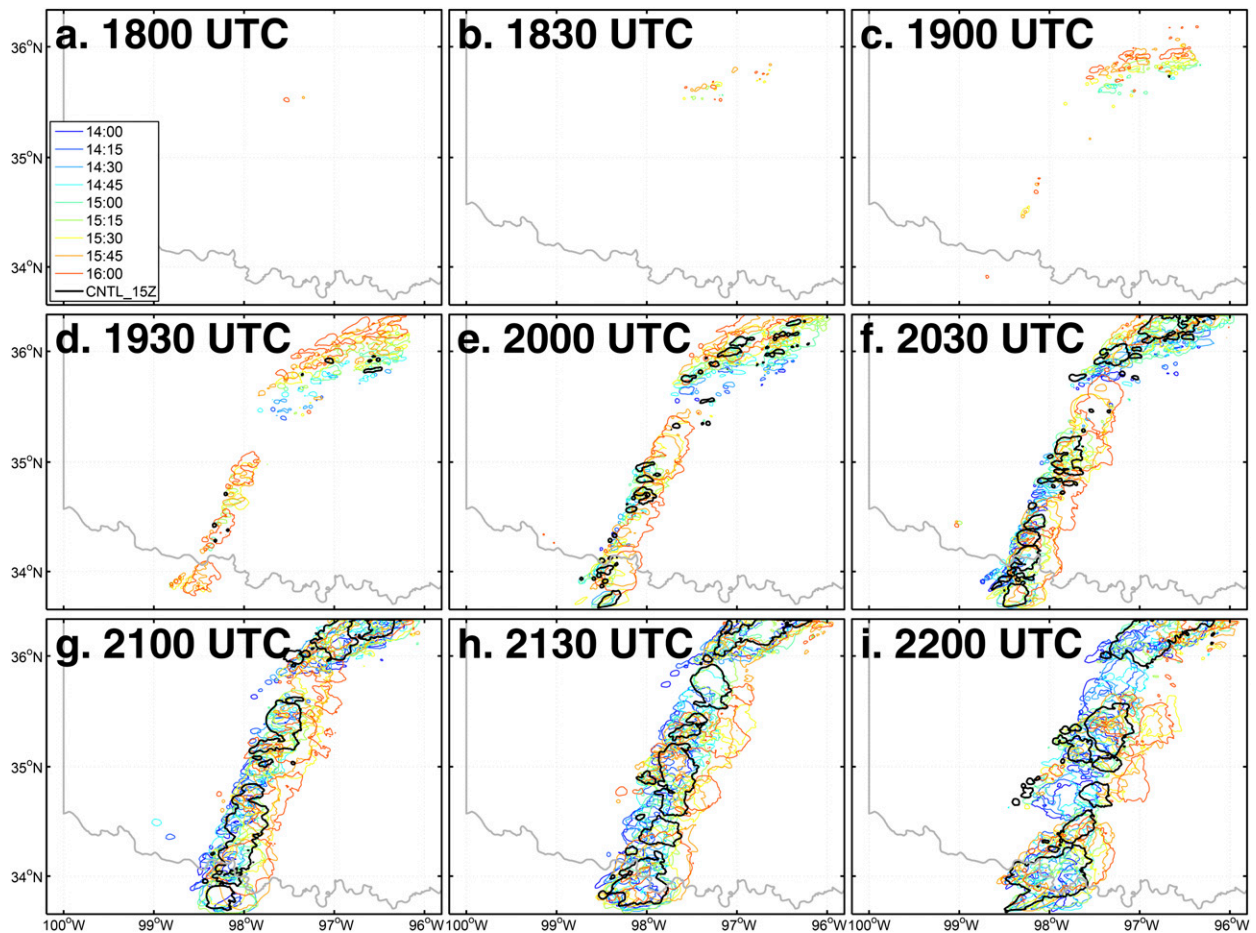


FIG. 5. Ensemble spaghetti plots of 40-dBZ composite reflectivity contours of the TIME\_SHIFT experiment from 1800 to 2200 UTC every 30 min.

an identical manner; there was no need to have a buffer zone near the boundaries of D04 since they perfectly coincided with the topography in D03. The terrain of the four shifted simulations in D04 is shown in Fig. 3b. The differences between applied topography in each of the four simulations and the CNTL simulation are also shown in Figs. 3c–f. Since the topography in D04 generally slopes from west to east, it is clear from Figs. 3c–f that a westward (eastward) shift of topography will result in a decreased (increased) terrain height. Simulations of D03 and D04 were then initialized at 1200 and 1500 UTC 20 May, respectively, and extended until 0000 UTC 21 May, the same simulation period as CNTL. This experiment will be referred to as TOPO\_SHIFT, and their reference perfect-model simulation is CNTL.

### c. Performance of CNTL and CNTL\_15Z

We first examined CNTL to check if the numerical model can reasonably simulate the variety of convective activity over Oklahoma during this day. The movement

of the shortwave trough in CNTL was slower than that in the RAP analysis and thus located more to the west (Fig. 2b), while the surface low was a little deeper with cooler surface temperatures (Fig. 2d). The sharp gradient of moisture, indicating the position of the dryline, matched well with the RAP analysis (Fig. 2f), although the dryline bulge in southwestern Oklahoma was not captured by CNTL. The stripe of unstable air ahead of the dryline was well captured, although SB-CAPE did not exceed  $5000 \text{ J kg}^{-1}$  until later times. Synoptically, this simulation qualitatively reproduced the environmental conditions that were favorable for severe convective storms in advance for 30 h, although the heating and moistening processes and associated increase of instability during the morning diurnal cycle were delayed. These differences, primarily delays in synoptic conditions, revealed the limited practical predictability of this simulation due to errors in the model.

Radar echoes in CNTL were first observed around 1900 UTC, roughly 1 h later than observed CI. A distinct

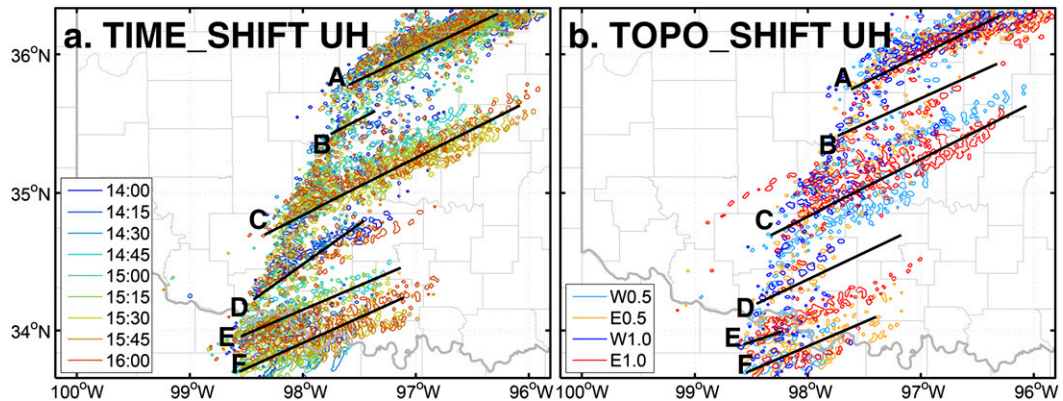


FIG. 6. Ensemble spaghetti plots of  $180 \text{ m}^2 \text{ s}^{-2}$  updraft helicity contours of (a) the TIME\_SHIFT experiment and (b) the TOPO\_SHIFT experiment. The black lines and accompanying letters indicate identified mesocyclone tracks of the CNTL\_15Z simulation in (a) and the CNTL simulation in (b) and are identical to those marked in Figs. 4b and 4a, respectively.

difference in the simulation compared to the observations was that convection initiated not only near the Oklahoma–Texas border but also to the northeast of Oklahoma City (Fig. 1b1). Numerous convective cells were triggered in each of the two areas of initial convection and new convection also formed in between, creating an eastward-moving broken line of storms by 2030 UTC (Fig. 1b3). Close inspection of the composite reflectivity field showed that the storms experienced complicated splitting and merging processes throughout the simulation (Figs. 1b4–b6). The simulated convection generally developed slower than the observed thunderstorms. After reaching maturity around 2100 UTC (Fig. 1b4), the overall quasi-linear organization weakened and the convective storms became more discrete than earlier (Figs. 1b5–b9), with some of the storms present until the end of the simulation.

With composite reflectivity values exceeding 65 dBZ, intense supercell thunderstorms represented by strong mesocyclones were expected. Mesocyclones were identified in the simulation using updraft helicity (UH; Kain et al. 2008) integrated over the 2–5-km layer AGL. A threshold was selected based on results of Naylor et al. (2012) for a numerical model with a horizontal grid spacing of 1 km, with UH values exceeding  $180 \text{ m}^2 \text{ s}^{-2}$  used to identify supercells. Results showed several mesocyclone tracks (labeled “A” to “F” in Fig. 4a), where the longest one originated around  $35^\circ\text{N}$ ,  $98^\circ\text{W}$  (track “C” in Fig. 4a) and was produced by one of the longest-lasting storms in the simulation. Although the 1-km resolution of D04 was unable to resolve tornadoes explicitly, the mesocyclone tracks indicated the potential for tornadoes to occur.

The general quasi-linear organization structure in CNTL\_15Z (Fig. 1c) was similar to CNTL, although

development of respective storms behaved differently with different characteristics in UH tracks (Fig. 4b): the storm related with track “B” dissipated rapidly, its track “D” oriented farther northward, and a more apparent and much longer track “E” occurred. Because the IC and model setting were identical for CNTL and CNTL\_15Z, the distinctions between these two simulations were solely introduced by their different LBC due to the cold start of D03 at 15Z of CNTL\_15Z, and also revealed the limited practical predictability of this event in another perspective.

#### 4. Impact of synoptic timing

In this section, the phrase “earlier members” will refer to the ensemble members whose ICs were generated using CNTL output from earlier times (i.e., 1500–1545 UTC), whereas “later members” will refer to ensemble members whose ICs were generated using CNTL output from later times (i.e., 1515–1600 UTC). The initiation and early development of convection in TIME\_SHIFT is shown in Fig. 5 using ensemble spaghetti plots from isolines of 40-dBZ composite reflectivity. It is apparent

TABLE 1. Success rate (%) of TIME\_SHIFT and TOPO\_SHIFT ensembles producing a supercell storm as identified by an updraft helicity track for storms A–E as shown in Fig. 5.

Track	TIME_SHIFT	TOPO_SHIFT
A	100	100
B	0	50
C	78	100
D	55	50
E	78	75
F	89	75

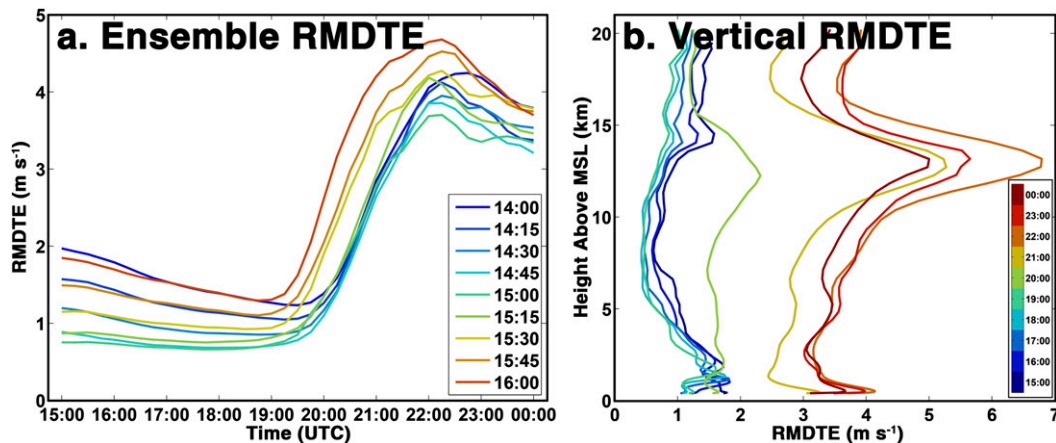


FIG. 7. (a) Domain-averaged and (b) horizontal-averaged RMDTE of the TIME\_SHIFT experiment.

from Fig. 5 that CI processes within D04 were time dependent with respect to different members. There was a clear delay of CI from later members to earlier members; for example, CI in the member of 1600 IC occurred around 1800 UTC in the northern region and 1900 UTC in the southern region (red contours in Figs. 5a and 5c), while CI in the member of 1400 IC occurred around 1930 UTC in the northern region and 2030 UTC in the southern region (blue contours in Figs. 5d and 5f). In other words, CI in the 1400 IC member were systematically delayed by approximately 2 h compared with the 1600 IC member throughout the whole D04.

The time shifting not only affected the timing of CI, but also changed the strength and track of individual storms. Examination of the UH tracks in this ensemble showed that several of the supercell storms were very predictable, while others were not (Fig. 6). This analysis followed the notion of success rates from Wandishin et al. (2008, 2010), in which one simply determines whether or not a storm is present in the ensemble. Results showed that the northernmost UH track (labeled A in Fig. 6) was predicted in every member of the ensemble (Table 1). In contrast, track B was not predicted in any of the TIME\_SHIFT ensemble members, although there were indications of occasionally higher UH values along its path in the ensemble spaghetti plot. The long track C was present in 78% of the members, as two of the earlier members failed to produce storms associated with this track, with CI shifted slightly to the north of CNTL\_15Z. Storm motion was slightly to the right of the CNTL\_15Z storm that associated with track C and storm motion turned more rightward for later members. Tracks D, E, and F that were located in the southern region also experienced divergence among ensemble members. Whereas storms associated with tracks A and C had similar CI locations in the ensemble, storms associated with tracks D, E, and F had different locations of CI. Furthermore,

some members apparently produced a track E that was apparently separated from track F, while some others failed to produce this track. This was likely resulted from the juxtaposition of the storms associated with tracks E and F that if they were initiated closer in distance, the one that produced E dissipated rapidly.

To quantify the differences between ensemble members and CNTL\_15Z, following the definition in Ehrendorfer et al. (1999) and applications in Zhang et al. (2006), Bei and Zhang (2007), Sippel and Zhang (2008), and Melhauser and Zhang (2012), difference total energy (DTE) of each ensemble member at each grid point was calculated as  $DTE = 0.5[u'^2 + v'^2 + (c_p/T_r)T'^2]$ , where  $c_p = 1004.9 \text{ J kg}^{-1} \text{ K}^{-1}$  is the heat capacity at constant pressure,  $T_r = 270 \text{ K}$  is a reference temperature for calculation, and  $u'$ ,  $v'$ , and  $T'$  were differences between an ensemble member and CNTL\_15Z for the two components of horizontal wind and the temperature at each grid point, respectively. The root-mean difference total energy (RMDTE) was calculated by taking the square root of DTE averaged through a horizontal level, a vertical column, the whole model domain, or all the ensemble members. RMDTE could be regarded as combining root-mean-square errors of both wind and temperature fields in their energy form. Figure 7a shows domain-averaged RMDTE of each ensemble member. RMDTE of the latest member with 1600 IC started to increase the earliest and the increase of RMDTE was gradually delayed in earlier members. These differences were attributed to the time-dependent CI in different members. Maximum values of RMDTE from all members were reached around 2200 UTC and began decreasing afterward. The rapid increase of RMDTE after CI was also revealed in the ensemble-averaged vertical distribution of RMDTE (Fig. 7b). Before 1900 UTC, there was no apparent increase of vertical RMDTE, and differences between TIME\_SHIFT simulations and

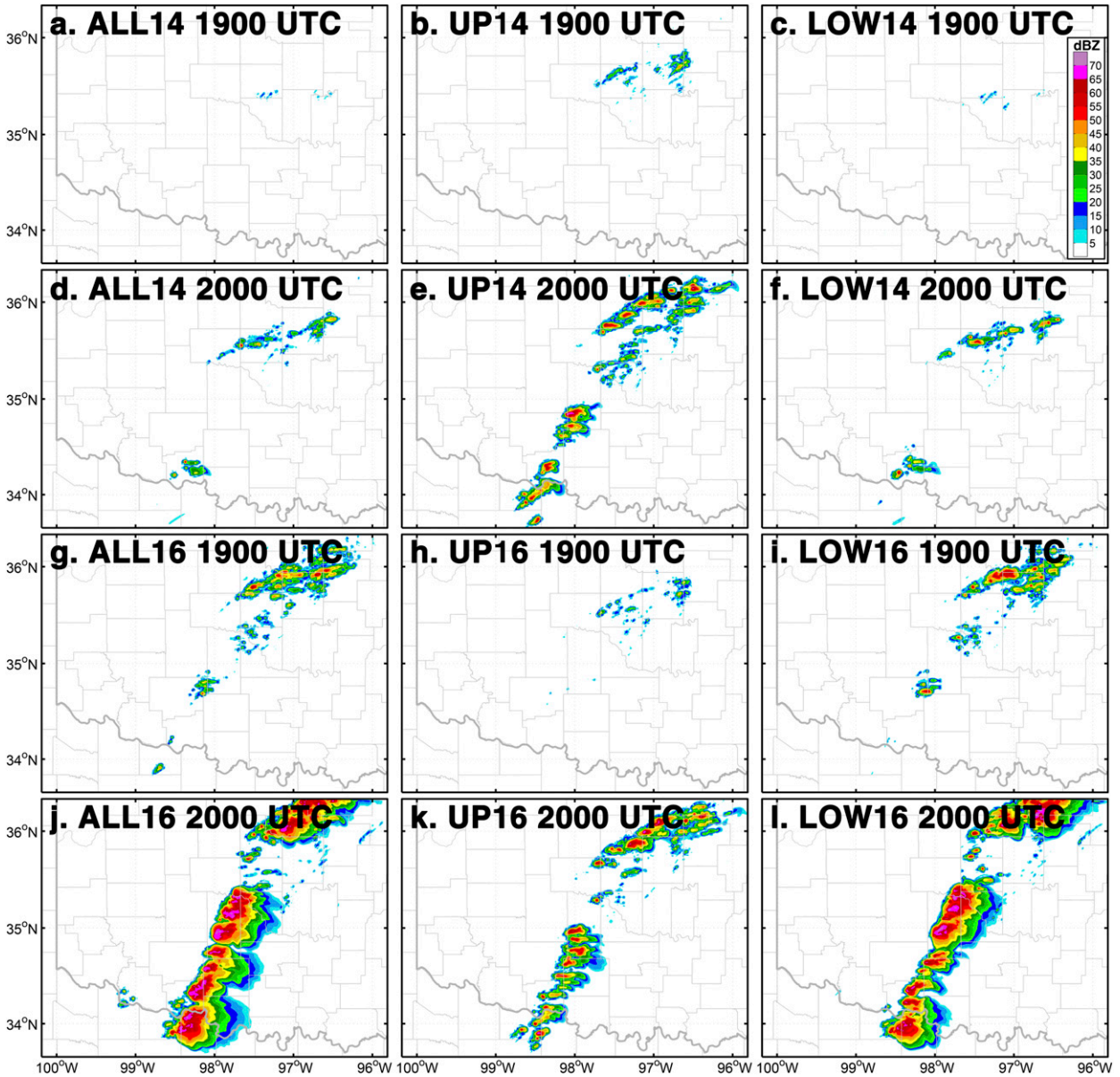


FIG. 8. Composite reflectivity of (a),(d) ALL14; (b),(e) UP14; (c),(f) LOW14; (g),(j) ALL16; (h),(k) UP16; and (i),(l) LOW16 at (a)–(c), (g)–(i) 1900 and (d)–(f),(j)–(l) 2000 UTC.

CNTL\_15Z were primarily concentrated in lower levels (<5 km), especially within the PBL (<1 km), and, to a smaller magnitude, upper levels (>10 km). As soon as convection began, RMDTE started to increase throughout the whole atmosphere, producing two local maxima, near the surface and tropopause, respectively, and then the RMDTE decreased after reaching its maximum value at all vertical levels at 2200 UTC.

Several additional paired sensitivity experiments were further performed to determine the source of the differences in CI timing. The first pair, UP14 and UP16, partially replaced the IC of CNTL\_15Z by the 1400 and

1600 ICs of TIME\_SHIFT. Model levels higher than 4 km AGL (around 600 hPa) were completely replaced by the 1400 and 1600 IC, while levels below 2.5 km AGL (around 700 hPa) remained unchanged as in CNTL\_15Z, and levels between 2.5 and 4 km AGL were transitioned by linearly combining ICs from CNTL\_15Z and TIME\_SHIFT (similar to the method used to generate the initial ICs of TIME\_SHIFT, but applied in the vertical). The other pair, LOW14 and LOW16, only replaced the vertical levels below 2.5 km AGL using 1400 and 1600 ICs, while the ICs above 4 km AGL were kept identical to CNTL\_15Z. Following a similar naming convention,

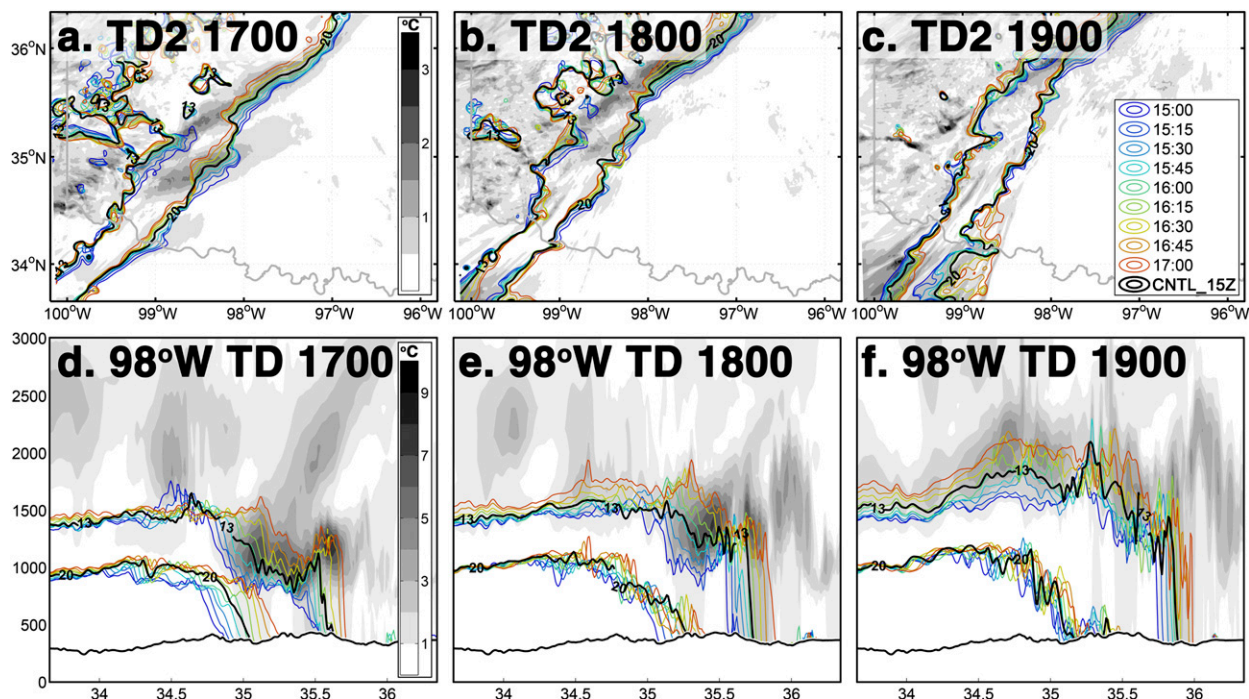


FIG. 9. Ensemble spaghetti of 13°C and 20°C isodrosotherms (colored lines) and ensemble spread (shaded; °C) of (a)–(c) surface 2-m and (d)–(f) meridional cross section at 98°W at (a),(d) 1700; (b),(e) 1800; and (c),(f) 1900 UTC for the TIME\_SHIFT experiment.

the original ensemble members with 1400 and 1600 IC will be referred as ALL14 and ALL16 in this specific comparison. The primary contribution to CI timing is easy to determine by comparing these six simulations and CNTL\_15Z. In Fig. 8, it is clear that ALL14 showed similar CI timing and location as in LOW14 (Figs. 8a and 8c), and this similarity also revealed when comparing ALL16 and LOW16 (Figs. 8g and 8i). This similarity was maintained through the whole simulations (Figs. 8d,f and 8j,l). On the other hand, storms in UP14 and UP16 (Figs. 8b,e,h,k, respectively) were distinct from ALL14/LOW14 and ALL16/UP16, while these two simulations were almost identical to each other (i.e., cf. Figs. 8b,e and 8h,k) as well as to CNTL\_15Z with only slightly differences in storm locations. These sensitivity experiments demonstrated that the differences in timing of CI in the TIME\_SHIFT ensemble were primarily due to the differences within lower levels of the troposphere in each member.

Several basic ingredients for deep moist convection (Johns and Doswell 1992; Doswell et al. 1996) were examined to determine how different ICs, especially the differences in lower levels as indicated by the sensitivity experiments shown earlier, influenced the timing of CI. Surface 2-m dewpoint  $T_d$  can be used to identify the location of the dryline. As also revealed by the synoptic analysis, there was a sharp horizontal gradient of

low-level moisture in Oklahoma where  $T_d$  changed by as much as 10°C in less than 100 km (Fig. 9a); this gradient became even sharper during the local afternoon right before CI occurred (Figs. 9b,c). The uncertainties of moisture were mainly located along this gradient as well as on the drier (west) side of the dryline, while in the moist (east) region the ensemble spread was much smaller (less than 0.5 K; Fig. 9c). At the same time, the low-level moisture within the PBL also became deeper for later ensemble members (Figs. 9d–f). The largest values of ensemble spread for  $T_d$  were located aloft rather than near the surface, indicating that the major differences in moisture between members were associated with the depth of the boundary layer. For example, the height of the 13°C isodrosotherm can differ by almost 1 km near 35.3°N at 1800 UTC for two ensemble members (Fig. 9e). A moisture difference of 1 g kg<sup>-1</sup> within the PBL was sufficient to discriminate between no initiation and severe convection in Crook (1996).

These differences in low-level moisture also affected environmental instability. All ensemble members had a northward extension of high most-unstable CAPE (MUCAPE) region, which resulted from the abundant moisture transport to the east of the dryline (Fig. 10). The successively earlier member isolines were located incrementally south of the 1600 IC member by a nearly constant distance (Figs. 10a–c). Larger ensemble spreads

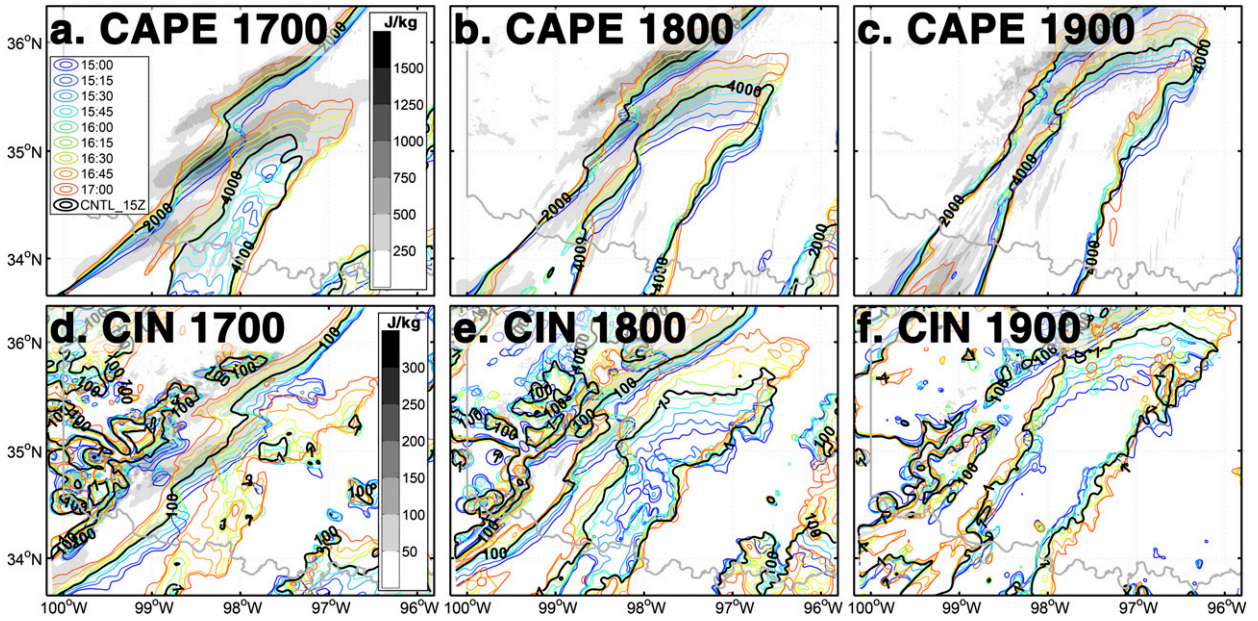


FIG. 10. Ensemble spaghetti contours (colored lines) and ensemble spread (shaded;  $J kg^{-1}$ ) of (a)–(c) 2000 and 4000  $J kg^{-1}$  MUCAPE and (d)–(f) 1 and 100  $J kg^{-1}$  MUCIN at (a),(d) 1700; (b),(e) 1800; and (c),(f) 1900 UTC for the TIME\_SHIFT experiment.

of MUCAPE were concentrated between the tip of the 4000 and the 2000  $J kg^{-1}$  isolines, indicating a dislocation of the northern tip of the 4000  $J kg^{-1}$  area. At 1800 UTC (Fig. 10b), when the later members already produced several convective cells with reflectivity exceeding 40 dBZ in the northern region, the MUCAPE in these members had already reached 4000  $J kg^{-1}$ , while the other members only had MUCAPE of over 2000  $J kg^{-1}$  at the same location. The most-unstable CIN (MUCIN) also had a similar southward progression for earlier members (Figs. 10d–f).

Some of the later members had reduced their MUCIN to below 1  $J kg^{-1}$  in central Oklahoma (Fig. 10d) by 1800 UTC, while for the earlier members same low value of MUCIN appeared 1 h later (Fig. 10e).

The differences in the vertical environmental structures were further examined by extracting simulated soundings from the ensemble forecast located at 35°N, 98°W, right in the center of the D04 domain. While using soundings at single grid points may raise representativeness issues, this problem was minor before CI as the

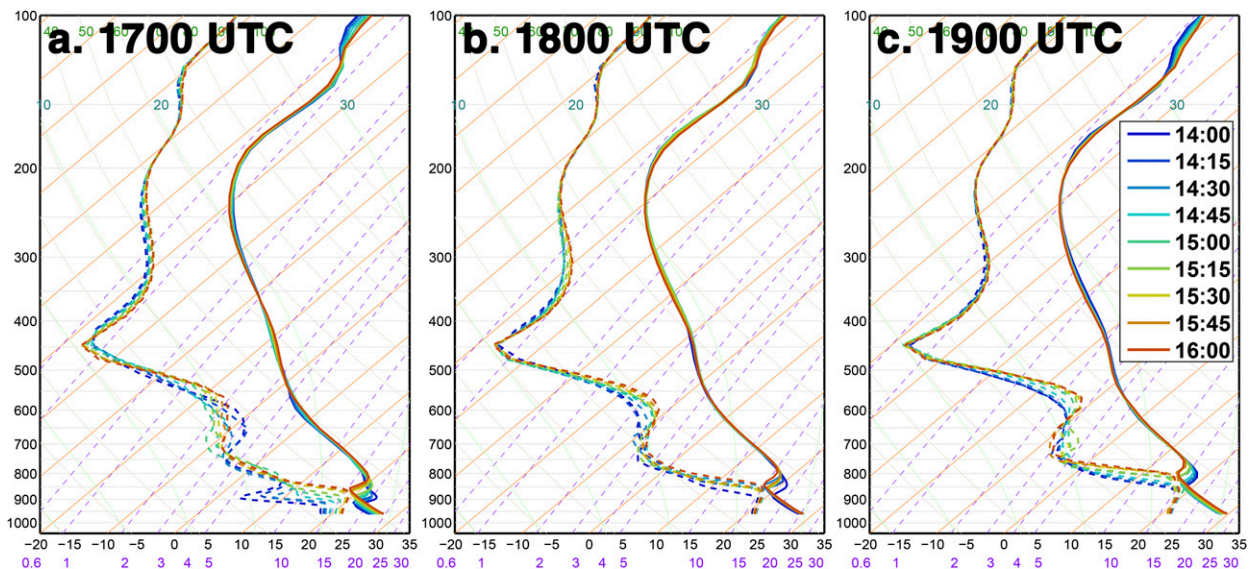


FIG. 11. Simulated sounding of the TIME\_SHIFT experiment located at 35°N, 98°W at (a) 1700, (b) 1800, and (c) 1900 UTC.

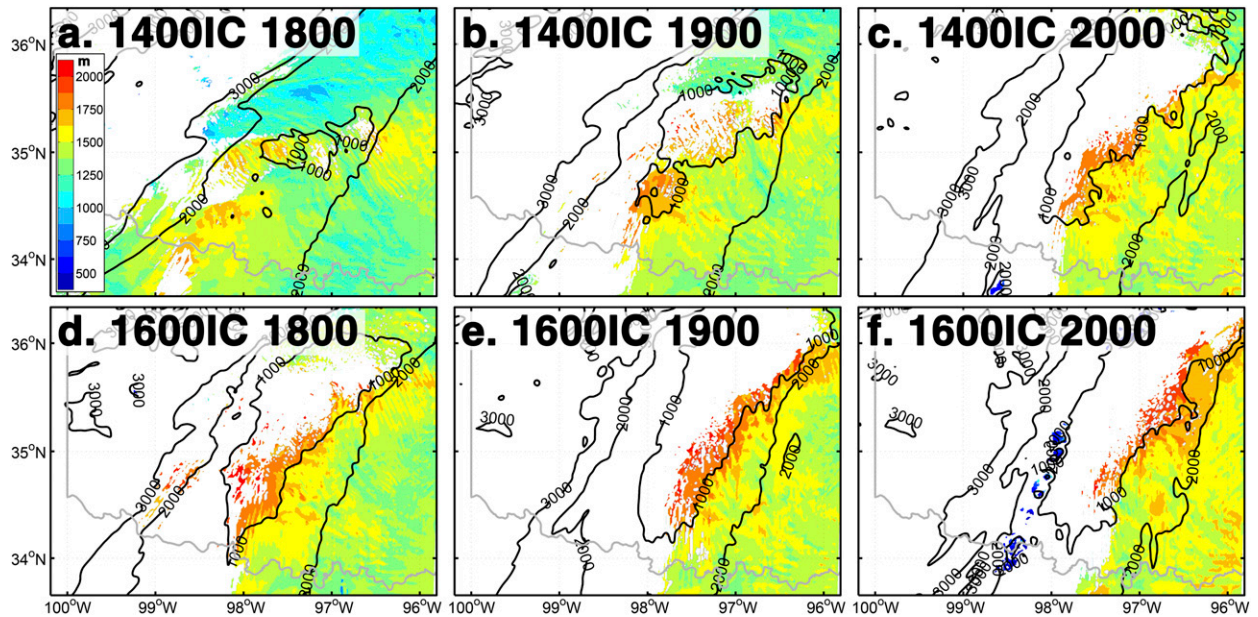


FIG. 12. Capping inversion height (shaded; m) and LFC height (contours, every 1000 m) for (a)–(c) 1400 IC member and (d)–(f) 1600 IC member of the TIME\_SHIFT experiment at (a),(d) 1800; (b),(e) 1900; and (c),(f) 2000 UTC.

atmosphere was more locally homogeneous than after CI. The differences in vertical structures of different ensemble members were most apparent in the moisture profiles below 500 hPa, with the later members being systematically more humid than the earlier members.

For example, at 1700 UTC (Fig. 11a), the 1600 IC member was already very moist, with air parcels around 850 hPa at the simulated sounding location nearly saturated, while for the 1400 IC the difference between temperature and dewpoint was as large as 20°C at a similar height since the

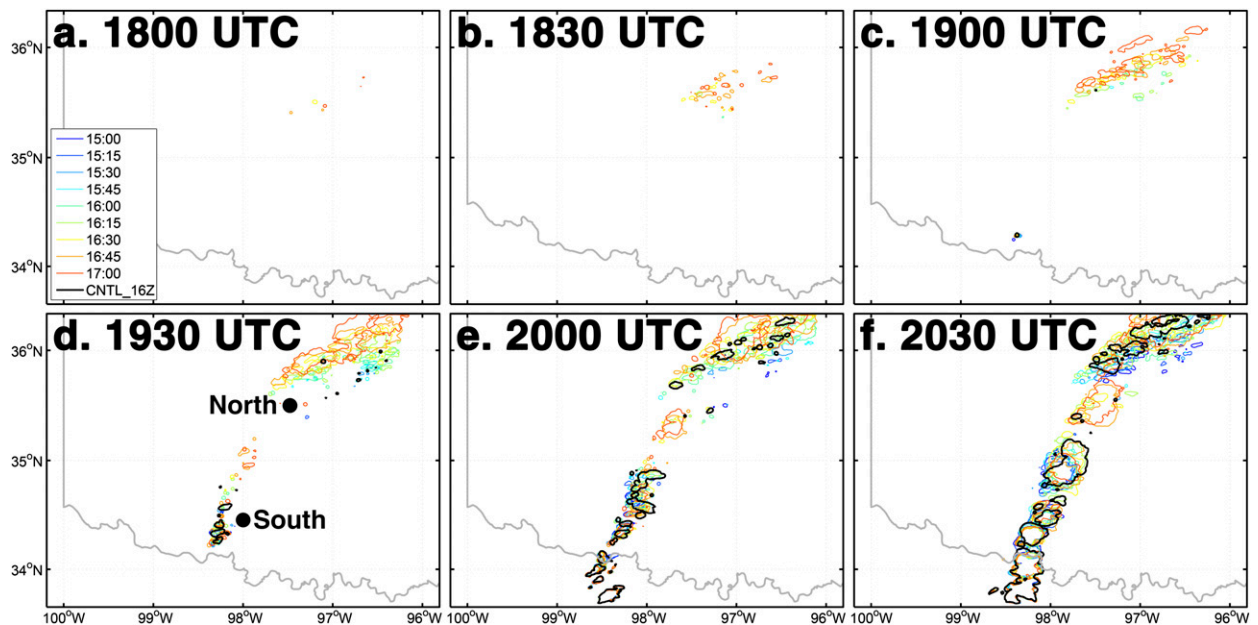


FIG. 13. Ensemble spaghetti plots of 40-dBZ composite reflectivity contours of the TIME\_D04 experiment from 1800 to 2030 every 30 min. The black dots in (d) indicate the locations of two soundings representing environments of the north and the south region in Fig. 15, respectively.

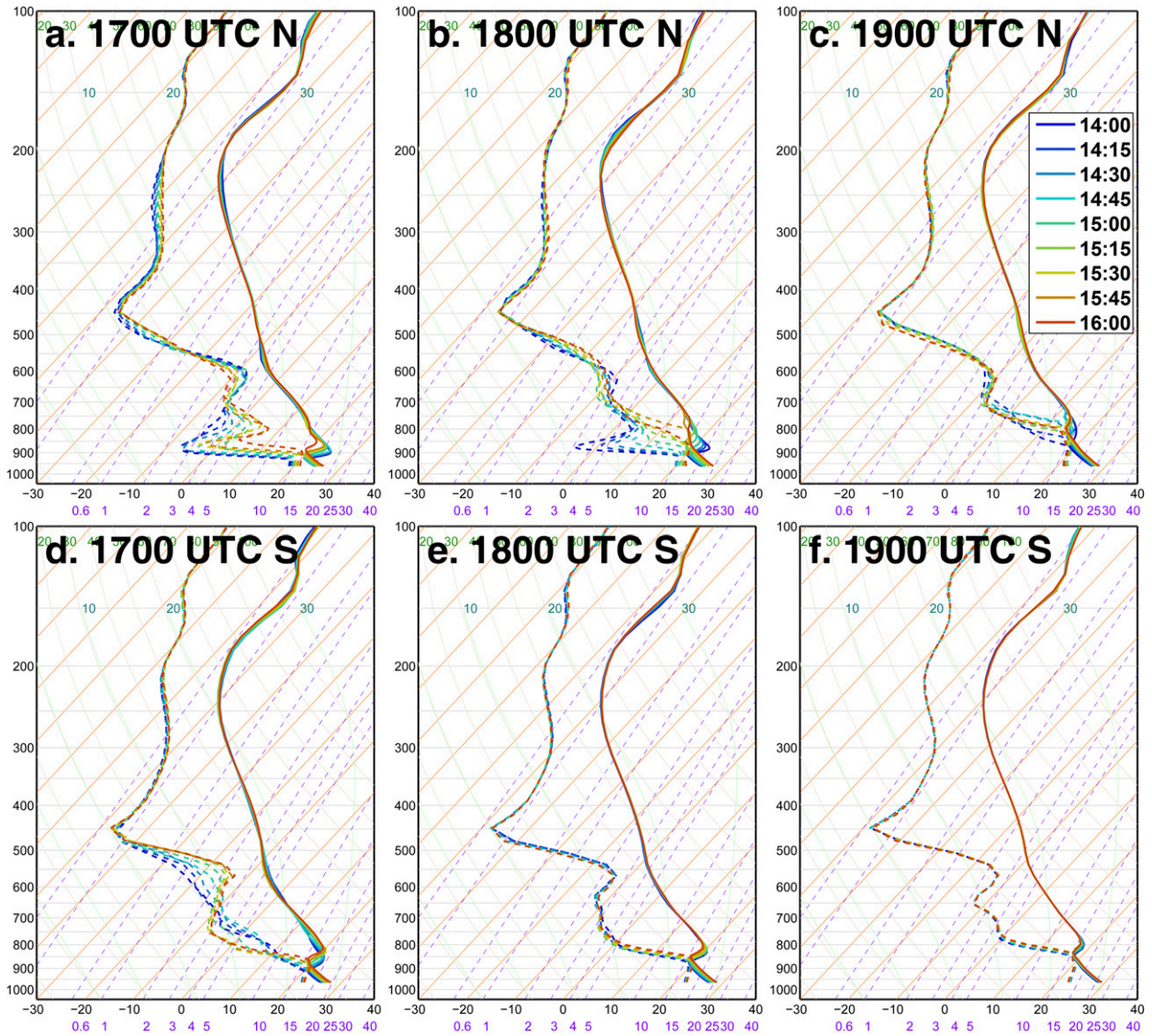


FIG. 14. Simulated sounding of the TIME\_D04 experiment located at (a)–(c) 35.5°N, 97.5°W (north sounding) and (d)–(f) 34.5°N, 98°W (south sounding) at (a),(d) 1700; (b),(e) 1800; and (c),(f) 1900 UTC.

northward expansion of moisture has not reached that location yet. The systematically drier PBL in the earlier member remained unchanged for the next several hours (Figs. 11b,c). The differences in the temperature profile were concentrated over a much shallower depth, with the later members showing a higher and weaker capping inversion, especially at 1900 UTC, and being warmer (colder) than the earlier members below (above) their capping inversions (Figs. 11a–c). The warmer and moister PBL in the later members resulted in higher CAPE and lower CIN than the earlier members.

The potential for CI in the ensemble members was also analyzed using the height of capping inversion and LFC. The inversion height was defined as the altitude of

the local maxima of the saturated wet bulb temperature profiles in the lowest 4 km AGL following Graziano and Carlson (1987). Only 1400 IC and 1600 IC members are presented in Fig. 12 for a clearer comparison. Values of LFC were generally higher in the 1400 IC member than the 1600 IC member before CI (Figs. 12a,b and 12d,e). Furthermore, the northern region in the 1600 IC member had no inversion at 1800 UTC (Fig. 12d), while the inversion was not removed until 2 h later (2000 UTC) in the same region in the 1400 IC member (Fig. 12c). Both the lower LFC height and the earlier removal of capping inversion in the 1600 IC member created an environment more favorable for CI than the 1400 IC member.

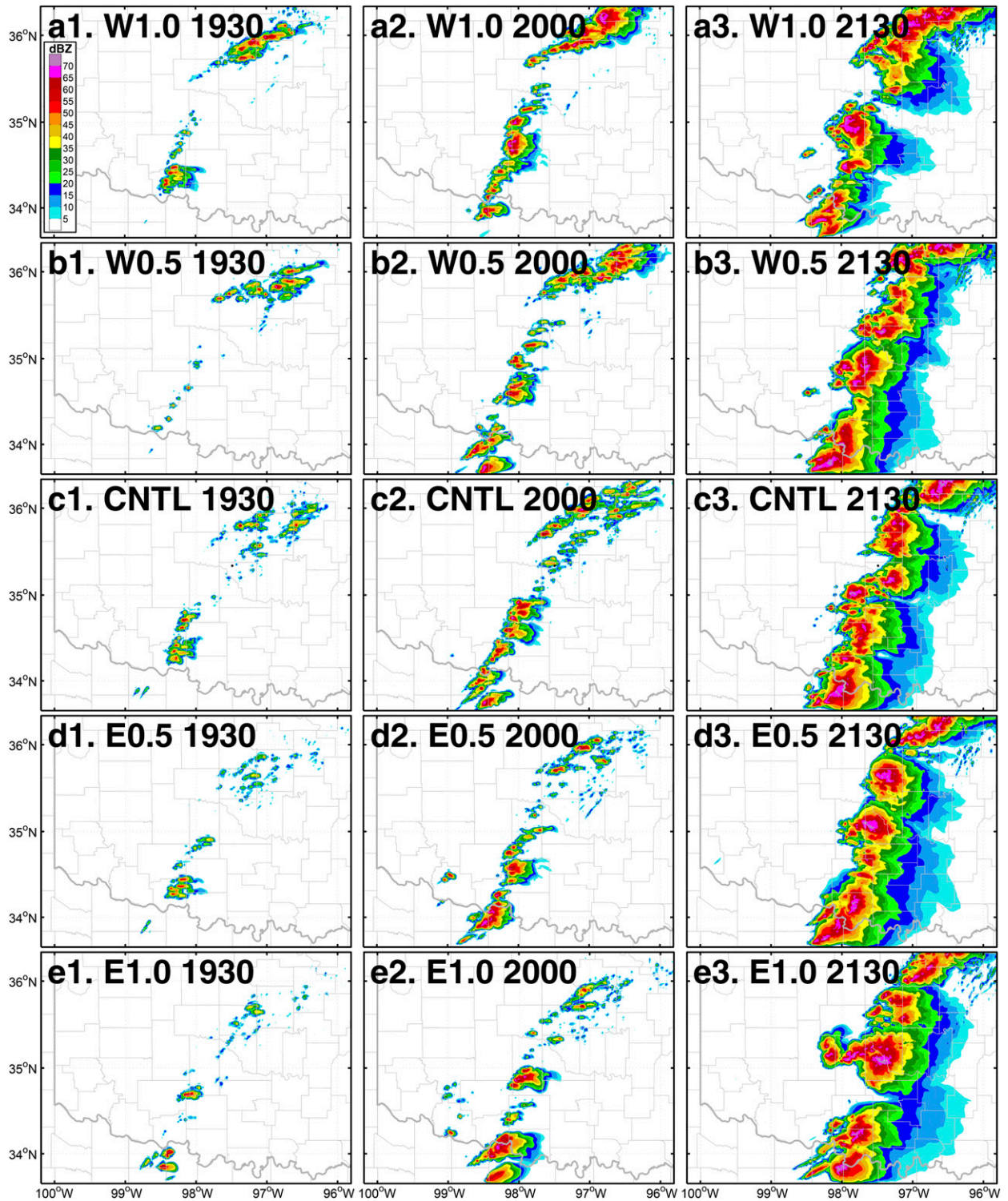


FIG. 15. Composite reflectivity of (a) W1.0, (b) W0.5, (c) CNTL, (d) E0.5, and (e) E1.0 simulations at (left) 1930, (middle) 2000, and (right) 2130 UTC.

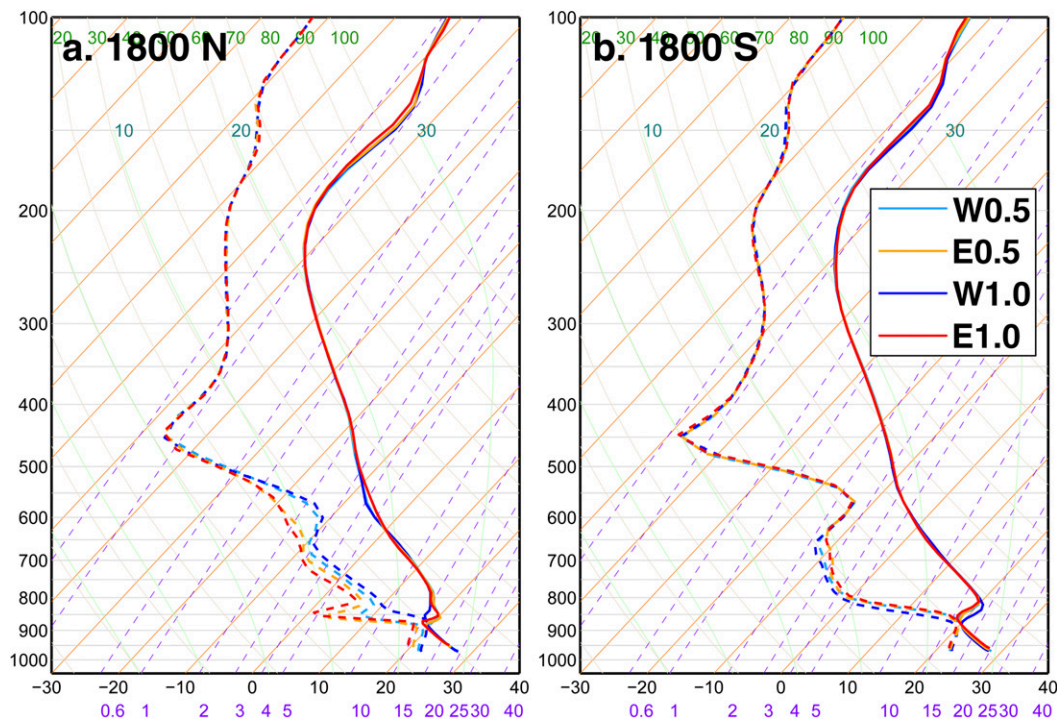


FIG. 16. Simulated sounding of the TOPO\_SHIFT experiment located at (a) 35.5°N, 97.5°W (north sounding) and (b) 34.5°N, 98°W (south sounding) at 1800 UTC.

Previous analyses showed that the timing of CI generally synchronized with the timing of their ICs. An additional ensemble forecast was performed to test the influence of unperturbed LBCs. This ensemble forecast, TIME\_D04, was similar to TIME\_SHIFT, but the shifting of ICs was performed only on D04. The 1500–1700 UTC outputs of CNTL were processed in a similar manner as TIME\_SHIFT with a 50-grid buffer zone and recentered at the 1600 UTC output. As expected, in this ensemble forecast CI timing in D04 were bifurcated into two regions: in the region roughly to the north of 35°N, CI were generally similar to TIME\_SHIFT that later members initiated earlier, while in the region to the south of 35°N, convections were initiated almost simultaneously around 1900 UTC (Fig. 13). Two soundings located at 34.5°N, 98°W and 35.5°N, 97.5°W representing southern and northern regions, respectively, were extracted to examine evolutions of environment conditions of these two regions (Fig. 14; sounding locations are indicated in Fig. 13d). It was apparent that the north sounding (Figs. 14a–c) showed similar characteristics as the TIME\_SHIFT sounding (Fig. 11) that later members were systematically more moist in lower levels and the capping inversion in the 1700 IC were already removed as of 1800 UTC (Fig. 14b). On the contrary, although at 1700 UTC there were still differences in vertical structure in different members (Fig. 14d), these differences decreased

quickly and at 1900 UTC just before CI both temperature and moisture profiles of all ensemble members became almost identical. Analysis of DTE proved this loss of ensemble spread in the southern region (figure not shown), which were contributed by the deterministic LBCs and the dominant southerly flows to the east of the dryline; in the original TIME\_SHIFT experiment, the distance between the southern boundaries of D03 and D04 avoided the aforementioned two factors from influencing environmental conditions within D04. This bifurcation of CI timing in TIME\_D04 not only showed the sensitivity of CI timing to the environmental conditions within the PBL, but also highlighted the importance of perturbing LBCs together with ICs in ensemble forecasts and ensemble-based data assimilation.

## 5. Influence from topography

The influence from topography on incorrectly predicted thunderstorms was explored in a reversed way so that terrain, instead of atmospheric conditions, was shifted. As stated earlier as well as shown in Fig. 3, a westward (eastward) shift of topography resulted in a decreased (increased) terrain height in this model domain setting. These changes in topography may also have an impact on CI and the development of severe convective storms. Results from the TOPO\_SHIFT ensemble showed that

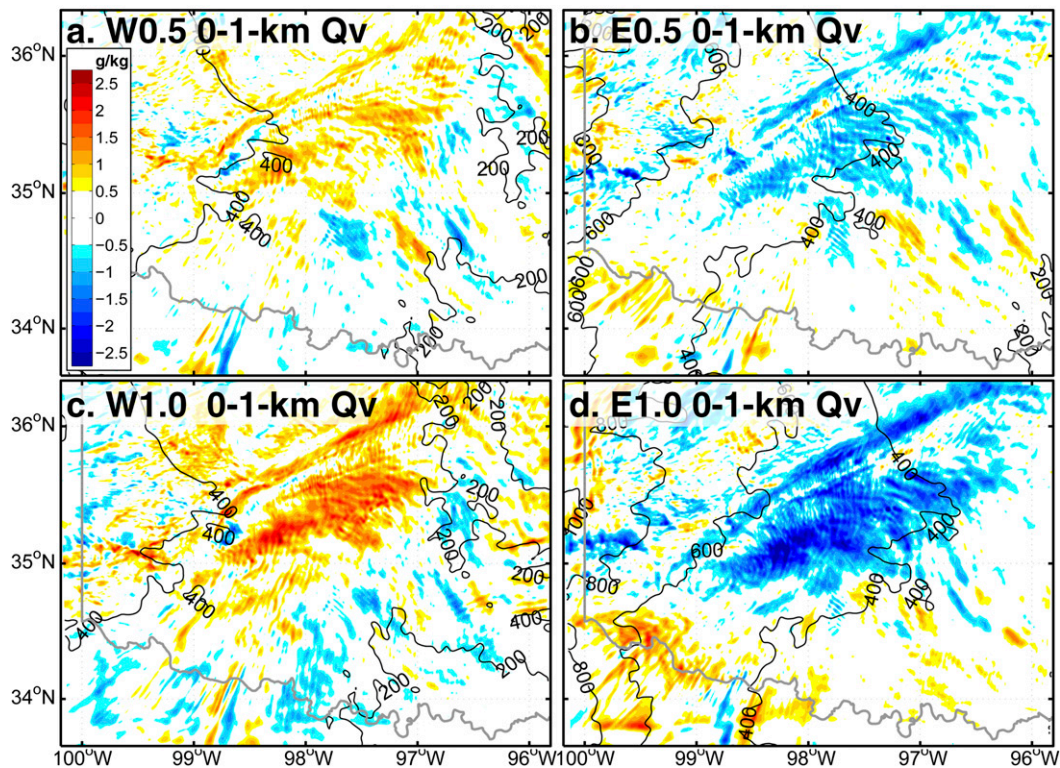


FIG. 17. Differences of 1515–1800 UTC 0–1-km mass-weighted average water vapor mixing ratio ( $Q_v$ ) change (shaded;  $\text{g kg}^{-1}$ ) of (a) W0.5, (b) E0.5, (c) W1.0, and (d) E1.0 compared with CNTL. Terrain height was plotted in contours (every 200 m).

there was a preference in timing of CI due to the terrain shift. In simulations with the terrain moved westward (W0.5 and W1.0), convection first initiated in both the northern and the southern regions (Figs. 15a1 and 15b1), whereas in simulations with the terrain moved eastward (E0.5 and E1.0), convection first initiated in the southern region (Figs. 15d1,e1). Although convection developed quickly in all simulations and formed into a quasi-contiguous convective line, the terrain changes altered the organizational mode (Figs. 15a3,b3,d3,e3). In W0.5 and E0.5 (Figs. 15b3,d3), there were numerous convective cells all closely collocated with each other and showing only small gaps of weaker stratiform precipitation in between the cells. This convective structure was very similar to CNTL (Fig. 15c3). However, as the topography shift became larger, the convective cells became more discrete and formed into a few very large storms (Figs. 15a3 and 15e3), especially in E1.0 (Fig. 15e3). This organizational difference resulted in a larger spread in the UH tracks compared with TIME\_SHIFT, especially along track C that had a width of more than  $0.5^\circ$  meridionally for TOPO\_SHIFT (Fig. 6b). Midlevel rotation was weaker in W1.0 along tracks B and C. In addition, storms in E0.5 and W1.0 also had a larger northward translation

component, producing the most deviant storm motions of  $235^\circ$ , a full  $10^\circ$  to the left of the storms in CNTL. In contrast, midlevel rotation in E1.0 was stronger and a larger and longer track C and E resulted from its extremely large and intense storm. Similar to the TIME\_SHIFT ensemble, storms A and C were still highly predictable with success rate of 100%, while storms B and D were the least predictable ones (Table 1).

The raising and lowering of topography undoubtedly changed the environmental thermodynamic properties near the surface due to the first law of thermodynamics. Two simulated environmental soundings were extracted at the same locations as in the TIME\_SHIFT experiment (Fig. 16). It was clear that for all four simulations at both the northern and southern region, temperature profiles were almost identical below their respective capping inversion (superimposed on each other), indicating that changes in topography did not alter the temperature structure within the PBL. However, large differences were observed in the moisture profile in the northern sounding (Fig. 16a). Simulation W1.0 produced the moistest PBL of the four simulations that almost saturated below its capping inversion at 1800 UTC and led to the lowest LFC around 900 hPa as well as the largest

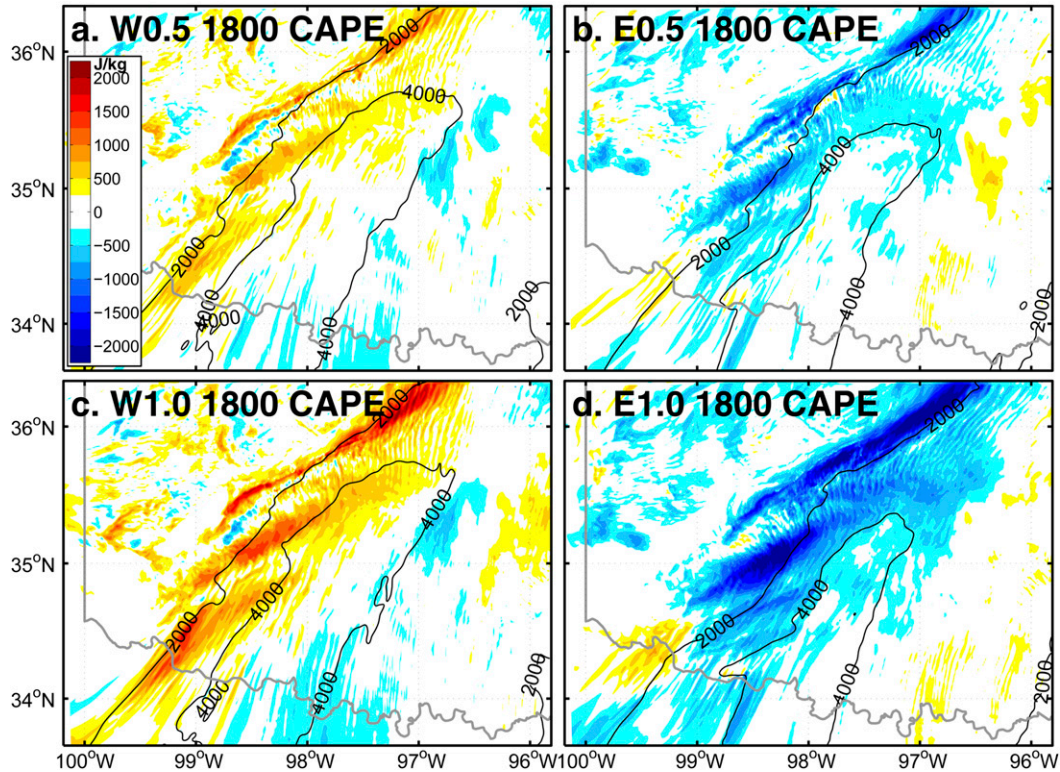


FIG. 18. MUCAPE (contours, every  $2000 \text{ J kg}^{-1}$ ) and its differences from CNTL (shaded;  $\text{J kg}^{-1}$ ) for (a) W0.5, (b) E0.5, (c) W1.0, and (d) E1.0 at 1800 UTC.

MUCAPE, whereas the driest E1.0 PBL had the highest LFC around 750 hPa and the smallest MUCAPE (instability will be analyzed shortly after). However, the differences in dewpoint profiles in the southern region (Fig. 16b) were much smaller than those in the northern region.

To further reveal the differences in moisture in the four simulations of TOPO\_SHIFT, we explored the changes in low level (within 1 km AGL, or roughly the PBL) moisture prior to CI from 1500 to 1800 UTC, focusing on the moistening process during the morning diurnal cycle and using mass-weighted averages. In this 3-h period, water vapor changes in TOPO\_SHIFT had localized biases in the four simulations. Large moisture differences were located to the north of  $35^\circ\text{N}$  in all simulations (Fig. 17), and in W1.0 and E1.0 the difference in magnitude was larger (Figs. 17c,d). The area of largest differences moved as the simulations advanced in time, although this area of largest differences was located in the same spot in all four simulations. Given this characteristic collocation, the drier PBL in W0.5 and W1.0 and the moister PBL in E0.5 and E1.0 during the morning diurnal cycle, consistent with their respective vertical profiles (Fig. 16), should be primarily due to thermodynamic responses to changes in terrain height.

Because of the changes of low-level moisture, large differences in environmental instability occurred among simulations of TOPO\_SHIFT. For example, the area of  $4000 \text{ J kg}^{-1}$  MUCAPE in W1.0 already approached  $36^\circ\text{N}$  as of 1800 UTC (Fig. 18c), while in E1.0 the same MUCAPE values were located almost  $0.5^\circ$  farther to the south (Fig. 18d). This  $2000 \text{ J kg}^{-1}$  difference in MUCAPE occurred in the same region where CI developed earlier in W1.0 than in E1.0. Similar trends of instability changes, but with smaller magnitudes, were also seen in W0.5 and E0.5 (Figs. 18a,b).

The modifications to the thermodynamic fields due to changes in topography primarily had an impact on low-level moisture, leading to different timing for CI. This result further confirmed the importance of low-level moisture to CI as what have already been observed in the TIME\_SHIFT experiments. On the other hand, the location of CI and the subsequent development and organization of convection were determined by dynamical processes (i.e., the wind field and its vertical structures) under favorable environmental conditions [e.g., Weisman and Klemp (1982, 1984); chapters 8 and 9 of Markowski and Richardson (2010)]. Three parameters related to the wind fields were considered here, representing low-level changes in mean wind, the vertical structure of wind, and

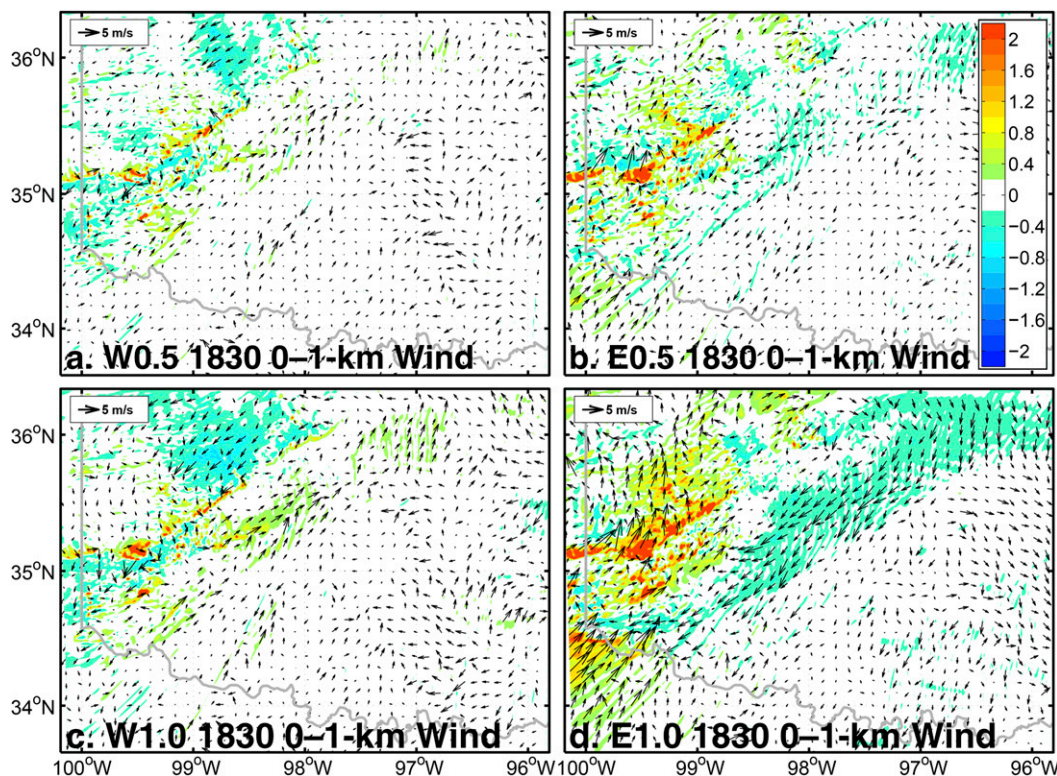


FIG. 19. Relative change of wind speed (shaded; times with respect to CNTL) and vector difference of wind (vectors) for 0–1-km mass-weighted average wind field of (a) W0.5, (b) E0.5, (c) W1.0, and (d) E1.0 compared with CNTL at 1830 UTC.

the vertically integrated effect of wind, respectively. Since the wind field was changing rapidly during the simulation, we only took one time point as a representative to explore how those parameters were enhanced in each of the simulations.

As already indicated by the strongly collocated area of large differences in moisture, there were no apparent regionally systematic modifications to the low-level wind fields within the region where convection was possible (i.e., to the east of the dryline). Changes of 0–1-km mass-weighted average wind speed in TOPO\_SHIFT compared with CNTL were about  $3 \text{ m s}^{-1}$  at 1830 UTC when convection was about to initiate (Fig. 19), which appeared small. However, there were large regions that showed vector differences of nearly  $5 \text{ m s}^{-1}$  but contained small changes in wind speed, indicating local turnings of wind direction that might have had an important impact on low-level convergence within the PBL. As a consequence, the low-level convergence in simulations was influenced (Fig. 20). During the hour right before CI, convergence within the lowest 1 km AGL in regions that MUCAPE exceeded  $4000 \text{ J kg}^{-1}$  in W0.5 and W1.0 simulations had been consistently wider spread than those in E0.5 and E1.0, especially to the north of  $35^\circ\text{N}$  after 1830 UTC

(Figs. 20c,d). The differences in low-level convergence might have contributed to the aforementioned phenomenon that in E0.5 and E1.0 CI occurred earlier in regions to the south of  $35^\circ\text{N}$  than to the north (Figs. 15d1,e1).

Another contribution to the enhancement of low-level convergence was changes in vertical wind shear. The 0–1-km vertical wind shear (referred to simply as “shear” hereafter) at 1830 UTC was examined to determine potential changes in the vertical structure of the wind field. Results indicated that large local changes in shear occurred, with the TOPO\_SHIFT simulations increasing the shear by more than two times in some places (Fig. 21). Although the majority of wind shear changes were concentrated on the drier side of the dryline, some of the very large changes were located on the moist side where convection was possible. There were also locations that, similar to what was observed for the 0–1-km mean wind previously, had small change in shear magnitude but large vector differences [e.g., around  $35.5^\circ\text{N}$ ,  $97^\circ\text{W}$  in E1.0 (Fig. 21d) where magnitude decreased by about 50% but vector differences were more than  $5 \text{ m s}^{-1}$ ], indicating local veering of the low-level wind shear. Although these changes of wind shear magnitude and direction were not

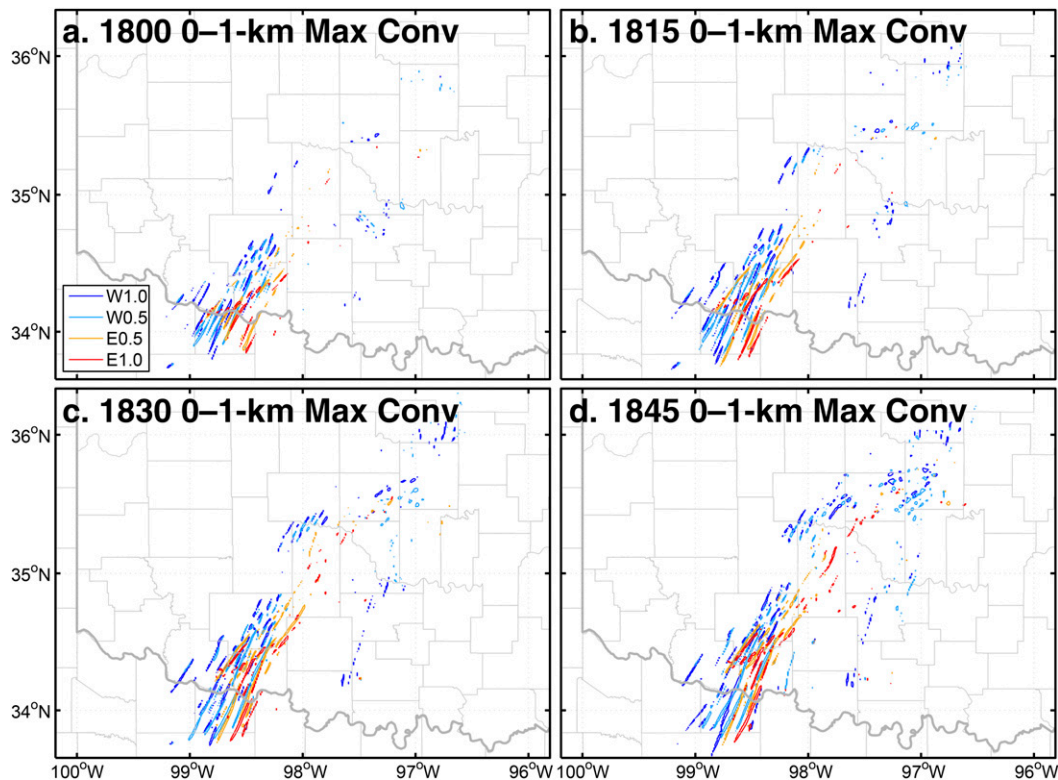


FIG. 20. The  $0.0015 \text{ s}^{-1}$  isoline of maximum convergence within the lowest 1 km AGL in regions that MUCAPE exceeds  $4000 \text{ J kg}^{-1}$  for the TOPO\_SHIFT simulations at (a) 1800, (b) 1815, (c) 1830, and (d) 1845 UTC.

large, they might enhance low-level convergence as seen for changes in the mean wind. In addition, changes in low-level shear magnitude might influence the type of convective cells that formed (Thompson et al. 2003) and lead to different structures of convection within the simulations.

Another dynamical parameter that is known to be essential for convection organization is the storm-relative environmental helicity (SREH; Davies-Jones et al. 1990; Markowski et al. 1998). Figure 22 shows the 0–3-km low-level SREH for the four simulations at 2000 UTC during the development of convection. It was clear that SREH around the convective region in all simulations was between  $100$  and  $150 \text{ m}^2 \text{ s}^{-2}$ . However in regions more to the east that influenced convection later in the day, larger variability were observed: in E1.0, SREH only exceeded  $150 \text{ m}^2 \text{ s}^{-2}$  and E0.5 (Figs. 22b,d) was only slightly higher and barely exceeded  $200 \text{ m}^2 \text{ s}^{-2}$ ; while in W0.5 and W1.0, SREH of  $200 \text{ m}^2 \text{ s}^{-2}$  was present in large areas (Figs. 22a,c). These larger differences in SREH indicate that, although the direct dynamical influence of changes in topography is small, when integrated over some depth it can be sufficient to modify parameters known to be relevant to storm structure and evolution.

## 6. Summary

The Moore, Oklahoma, EF-5 tornado on 20 May 2013 was one of the deadliest and costliest tornadoes in the United States in recent years. Focusing on the convective development and storm evolution on this day, this work explored the practical predictability of severe convective thunderstorms with respect to changes in synoptic timing, boundary layer development, and topographical influence by utilizing the WRF-ARW Model with a convection-permitting horizontal grid spacing of 1 km.

The control deterministic simulation (CNTL) was initialized at 1200 UTC 19 May 2013 (about 30 h prior to convection initiation) using the GFS analysis and forecast and successfully predicted the environmental conditions including the upper-level flow pattern, the shortwave trough to the west of Oklahoma, the low-level moisture transport from the Gulf of Mexico, the dryline across Oklahoma, and the extremely unstable air to the east of the dryline in Oklahoma. The CNTL simulation had minor discrepancies when compared to the RAP analysis. The timing and location of CI were in close agreement to those observed by the WSR-88Ds, although later on the development of the simulated convection was not as

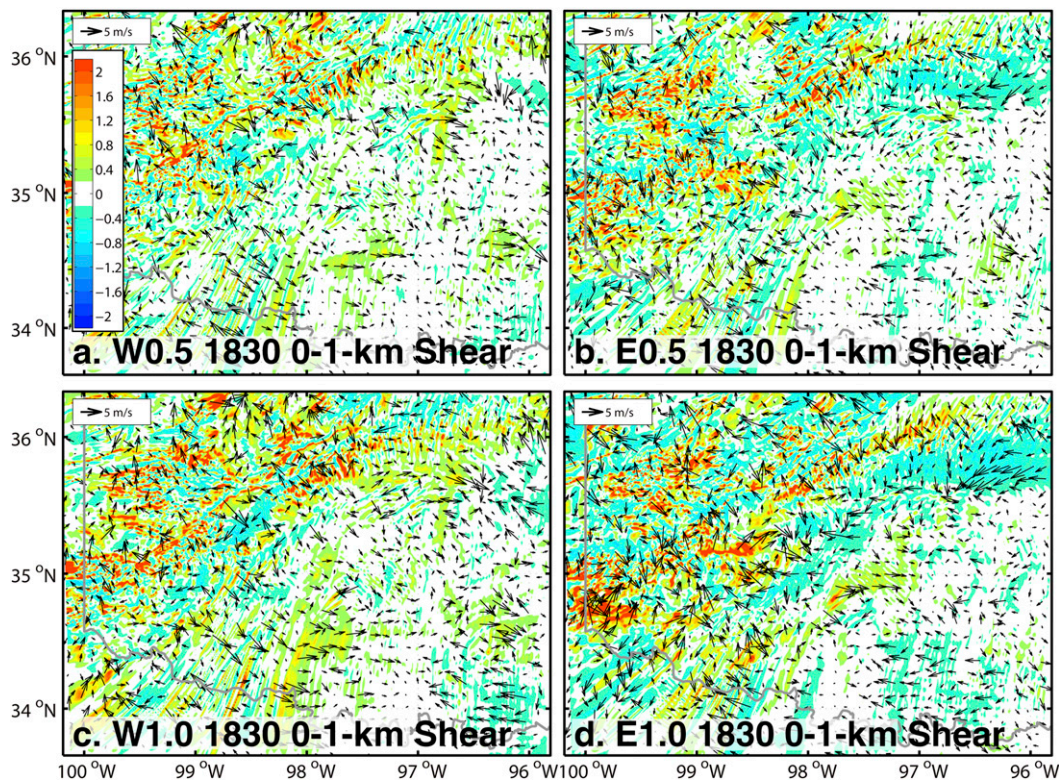


FIG. 21. Relative change of wind shear magnitude (shade; times with respect to CNTL) and vector difference of wind shear (vectors) for 0–1-km vertical wind shear of (a) W0.5, (b) E0.5, (c) W1.0, and (d) E1.0 compared with CNTL at 1830 UTC.

rapid as the actual thunderstorms and the organization in CNTL was more contiguous than observed. The multiple mesocyclone tracks, indicated by large values of 2–5-km UH, implied the possibility of tornadoes in some of the simulated storms.

Two error sources in severe thunderstorm prediction practices were considered in this study: those from delay or advancing in synoptic conditions of global model forecasts, and those from location discrepancies of initiated convections in numerical models. The TIME\_SHIFT ensemble focused on the impact of synoptic timing on differences in boundary layer development. Results showed that the initiation of convection in the ensemble generally synchronized with their respective ICs. For the members with ICs using CNTL outputs of later times, favorable convective conditions were reached earlier, including more moisture within the PBL, larger instability (greater CAPE) and weaker inhibition (less CIN, lower LFC, and the earlier removal of capping inversion). This led to earlier CI than seen in those members using earlier CNTL outputs as ICs. Sensitivity experiments proved that the timing of CI was primarily influenced by changes within the lower levels of the troposphere. An additional set of simulations

using deterministic LBC for all ensemble members showed a bifurcation of CI timing in different regions. Convections in the southern region of D04 were initiated almost simultaneously among all members resulting from the influence of the LBC, further confirming the impact of synoptic timing of IC in creating a favorable environment for convection as well as the importance of perturbing LBCs in keeping well-spread ensembles during the forecast.

The TOPO\_SHIFT ensemble considered the effects of topography on spatially incorrectly initiated thunderstorms by directly moving the model terrain westward or eastward for  $0.5^\circ$  or  $1.0^\circ$ . Changing the topography modified not only the timing of CI but also the development and the organization of the simulated thunderstorms. Changes in terrain height altered the moisture and CAPE within the PBL, creating different environmental conditions in which convection initiated. While the terrain height changes did not systematically alter the overall flow pattern, the dynamical response of the wind fields to the smaller-scale topography details, such as hills and valleys, led to locally concentrated convergence via changes in wind speed, wind direction, or variations in vertical wind shear within the PBL. It

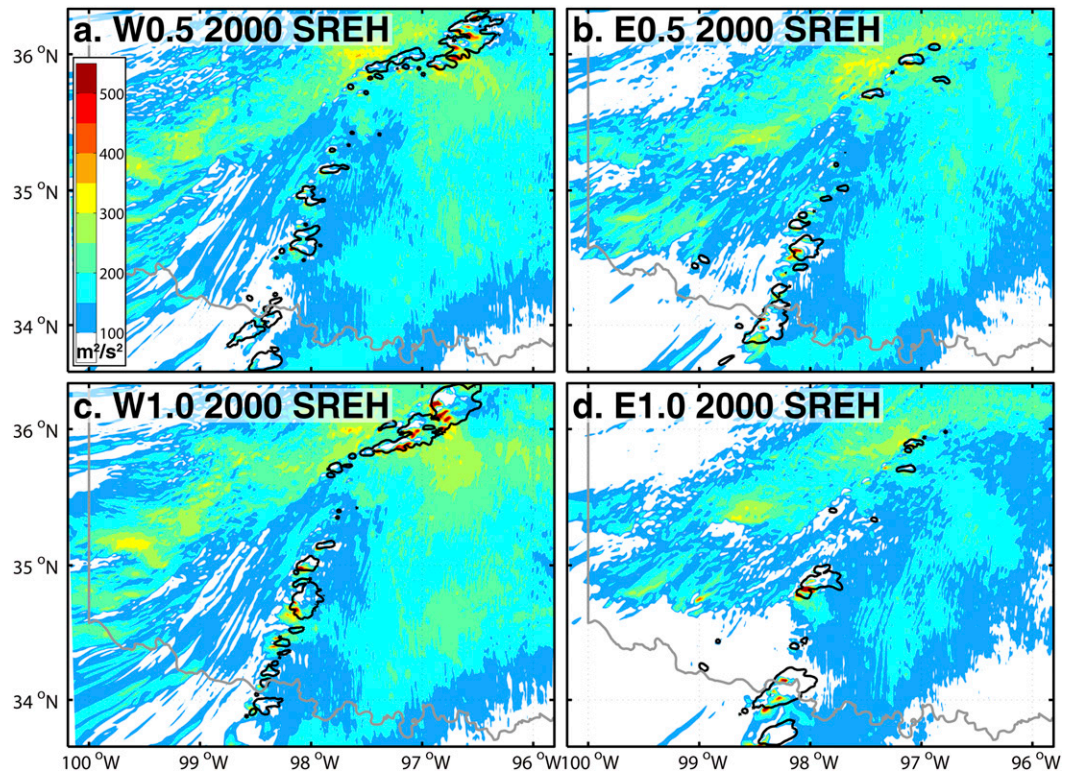


FIG. 22. Storm-relative helicity (shaded;  $\text{m}^2 \text{s}^{-2}$ ) and 40-dBZ composite reflectivity (contours) of (a) W0.5, (b) E0.5, (c) W1.0, and (d) E1.0 at 2000 UTC.

also changed the low-level SREH, which is a vertically integrated parameter. Under favorable environmental conditions, locally enhanced convergence may lead to CI in different locations, while the wind shear and SREH may influence the development and organization of subsequent convective storms.

These results indicated that errors in the prediction of the severe convective thunderstorms in Oklahoma on 20 May 2013 could be produced from changes in synoptic timing and topographical influence, primarily through their influence on the structure of the PBL. The changes in ICs applied for this study were comparable to analysis errors within current global models, implying a limited practical predictability for this event. This limitation was also revealed by the differences in the initiation and development of convection seen between CNTL and the observed thunderstorms. The conclusions in this study indicate further questions; for example, how to account for uncertainties associated with PBL parameterization schemes that could lead to huge differences in the structure of the PBL in deterministic and ensemble forecasts? Since practical predictability is strongly associated with current practices, our study suggests some possibilities in improving severe thunderstorm predictions in operations.

This work also revealed the importance of perturbing the LBCs when creating reasonably distributed ensembles for ensemble forecasting and data assimilation purposes. In addition, even when the differences between ensemble members were comparably small (e.g., the southern region of the TIME\_D04 simulations), the locations of CI and the subsequent development of the thunderstorms still showed varied characteristics and randomness among these members. This phenomenon suggests that uncertainties in predicting thunderstorms may remain even when model error is greatly reduced, such that their predictability is intrinsically limited. The intrinsic predictability of this event has been investigated and will be detailed in a future study, in which the impact of very tiny initial differences of two members that run with exact model configuration were examined.

*Acknowledgments.* Discussions with Christopher Melhauser and Jonathan Poterjoy benefited this work greatly. Yunji Zhang is supported by the Ministry of Science and Technology of China Grant 2013CB430104 and the Chinese Scholarship Council (CSC). Fuqing Zhang is supported by the Office of Naval Research Grant N000140910526 and the National Science Foundation

Grant AGS-1305798. David J. Stensrud is supported by the National Science Foundation Grant ATM-1230114. Zhiyong Meng is supported by the Ministry of Science and Technology of China Grant 2013CB430104 and the Natural Science Foundation of China Grants 41375048 and 41425018. The simulations were performed on the Texas Advanced Computing Center (TACC).

## REFERENCES

- Atkins, N. T., K. M. Butler, K. R. Flynn, and R. M. Wakimoto, 2014: An integrated damage, visual, and radar analysis of the 2013 Moore Oklahoma EF5 tornado. *Bull. Amer. Meteor. Soc.*, **95**, 1549–1561, doi:10.1175/BAMS-D-14-00033.1.
- Bei, N., and F. Zhang, 2007: Impacts of initial condition errors on mesoscale predictability of heavy precipitation along the Mei-Yu front of China. *Quart. J. Roy. Meteor. Soc.*, **133**, 83–99, doi:10.1002/qj.20.
- Benjamin, S. G., G. A. Grell, J. M. Brown, and T. G. Smirnova, 2004: Mesoscale weather prediction with the RUC hybrid isentropic-terrain-following coordinate model. *Mon. Wea. Rev.*, **132**, 473–494, doi:10.1175/1520-0493(2004)132<0473:MWPWTR>2.0.CO;2.
- Bluestein, H. B., and S. S. Parker, 1993: Modes of isolated, severe convective storm formation along the dryline. *Mon. Wea. Rev.*, **121**, 1354–1372, doi:10.1175/1520-0493(1993)121<1354:MOISCS>2.0.CO;2.
- Bright, D. R., and S. L. Mullen, 2002: The sensitivity of the numerical simulation of the southwest monsoon boundary layer to the choice of PBL turbulence parameterization in MM5. *Wea. Forecasting*, **17**, 99–114, doi:10.1175/1520-0434(2002)017<0099:TSOTNS>2.0.CO;2.
- Burgess, D., and Coauthors, 2014: 20 May 2013 Moore, Oklahoma, tornado: Damage survey and analysis. *Wea. Forecasting*, **29**, 1229–1237, doi:10.1175/WAF-D-14-00039.1.
- Chou, M.-D., and M. J. Suarez, 1994: An efficient thermal infrared radiation parameterization for use in general circulation models. NASA Tech. Memo. 104606, Vol. 3, NASA Goddard Space Flight Center, 84 pp.
- Cintineo, R. M., and D. J. Stensrud, 2013: On the predictability of supercell thunderstorm evolution. *J. Atmos. Sci.*, **70**, 1993–2011, doi:10.1175/JAS-D-12-0166.1.
- Coffer, B. E., L. C. Maudlin, P. G. Veals, and A. J. Clark, 2013: Dryline position errors in experimental convection-allowing NSSL-WRF model forecasts and the operational NAM. *Wea. Forecasting*, **28**, 746–761, doi:10.1175/WAF-D-12-00092.1.
- Colle, B. A., C. F. Mass, and D. Ovens, 2001: Evaluation of the timing and strength of MM5 and Eta surface trough passages over the eastern Pacific. *Wea. Forecasting*, **16**, 553–572, doi:10.1175/1520-0434(2001)016<0553:EOTTAS>2.0.CO;2.
- Coniglio, M. C., J. Correia Jr., P. T. Marsh, and F. Kong, 2013: Verification of convection-allowing WRF model forecasts of the planetary boundary layer using sounding observations. *Wea. Forecasting*, **28**, 842–862, doi:10.1175/WAF-D-12-01013.1.
- Crook, N. A., 1996: Sensitivity of moist convection forced by boundary layer processes to low-level thermodynamic fields. *Mon. Wea. Rev.*, **124**, 1767–1785, doi:10.1175/1520-0493(1996)124<1767:SOMCFB>2.0.CO;2.
- Davies-Jones, R. P., D. W. Burgess, and M. Foster, 1990: Test of helicity as a tornado forecast parameter. Preprints, *16th Conf. on Severe Local Storms*, Kananaskis Park, AB, Canada, Amer. Meteor. Soc., 588–592.
- Doswell, C. A., H. E. Brooks, and R. A. Maddox, 1996: Flash flood forecasting: An ingredients based methodology. *Wea. Forecasting*, **11**, 560–581, doi:10.1175/1520-0434(1996)011<0560:FFFAIB>2.0.CO;2.
- Ehrendorfer, M., R. M. Errico, and K. D. Raeder, 1999: Singular-vector perturbation growth in a primitive equation model with moist physics. *J. Atmos. Sci.*, **56**, 1627–1648, doi:10.1175/1520-0469(1999)056<1627:SVPGIA>2.0.CO;2.
- Elmore, K. L., D. M. Schultz, and M. E. Baldwin, 2006: The behavior of synoptic-scale errors in the Eta model. *Mon. Wea. Rev.*, **134**, 3355–3366, doi:10.1175/MWR3238.1.
- Gravelle, C. M., J. R. Mecikalski, W. E. Line, K. M. Bedka, R. A. Petersen, J. M. Sieglaff, G. T. Stano, and S. J. Goodman, 2015: Demonstration of a GOES-R satellite convective toolkit to “bridge the gap” between severe weather watches and warnings: An example from the 20 May 2013 Moore, Oklahoma, tornado outbreak. *Bull. Amer. Meteor. Soc.*, in press.
- Graziano, T. M., and T. N. Carlson, 1987: A statistical evaluation of lid strength on deep convection. *Wea. Forecasting*, **2**, 127–139, doi:10.1175/1520-0434(1987)002<0127:ASEOLS>2.0.CO;2.
- Grell, G. A., and D. Dévényi, 2002: A generalized approach to parameterizing convection combining ensemble and data assimilation techniques. *Geophys. Res. Lett.*, **29**, 1693, doi:10.1029/2002GL015311.
- Johns, R. H., and C. A. Doswell III, 1992: Severe local storms forecasting. *Wea. Forecasting*, **7**, 588–612, doi:10.1175/1520-0434(1992)007<0588:SLSF>2.0.CO;2.
- Kain, J. S., and Coauthors, 2008: Some practical considerations regarding horizontal resolution in the first generation of operational convection-allowing NWP. *Wea. Forecasting*, **23**, 931–952, doi:10.1175/WAF2007106.1.
- Lorenz, E. N., 1963: Deterministic nonperiodic flow. *J. Atmos. Sci.*, **20**, 130–141, doi:10.1175/1520-0469(1963)020<0130:DNF>2.0.CO;2.
- , 1969: The predictability of a flow which possesses many scales of motion. *Tellus*, **21A**, 289–307, doi:10.1111/j.2153-3490.1969.tb00444.x.
- , 1982: Atmospheric predictability experiments with a large numerical model. *Tellus*, **34A**, 505–513, doi:10.1111/j.2153-3490.1982.tb01839.x.
- , 1996: Predictability—A problem partly solved. *Proc. Seminar on Predictability*, Reading, United Kingdom, ECMWF, 1–18.
- Markowski, P. M., and Y. Richardson, 2010: *Mesoscale Meteorology in Midlatitudes*. Wiley-Blackwell, 407 pp.
- , J. M. Straka, E. N. Rasmussen, and D. O. Blanchard, 1998: Variability of storm-relative helicity during VORTEX. *Mon. Wea. Rev.*, **126**, 2959–2971, doi:10.1175/1520-0493(1998)126<2959:VOSRHD>2.0.CO;2.
- McNulty, R. P., 1995: Severe and convective weather: A central region forecasting challenge. *Wea. Forecasting*, **10**, 187–202, doi:10.1175/1520-0434(1995)010<0187:SACWAC>2.0.CO;2.
- Melhauser, C., and F. Zhang, 2012: Practical and intrinsic predictability of severe and convective weather at the mesoscales. *J. Atmos. Sci.*, **69**, 3350–3371, doi:10.1175/JAS-D-11-0315.1.
- Mlawer, E. J., S. J. Taubman, P. D. Brown, M. J. Iacono, and S. A. Clough, 1997: Radiative transfer for inhomogeneous atmospheres: RRTM, a validated correlated-k model for the longwave. *J. Geophys. Res.*, **102**, 16 663–16 682, doi:10.1029/97JD00237.
- Nakanishi, M., and H. Niino, 2009: Development of an improved turbulence closure model for the atmospheric boundary layer. *J. Meteor. Soc. Japan*, **87**, 895–912, doi:10.2151/jmsj.87.895.
- Naylor, J., M. S. Gilmore, R. L. Thompson, R. Edwards, and R. B. Wilhelmson, 2012: Comparison of objective supercell

- identification techniques using an idealized cloud model. *Mon. Wea. Rev.*, **140**, 2090–2102, doi:10.1175/MWR-D-11-00209.1.
- Rhea, J. O., 1966: A study of thunderstorm formation along drylines. *J. Appl. Meteor.*, **5**, 58–63, doi:10.1175/1520-0450(1966)005<0058:ASOTFA>2.0.CO;2.
- Roebber, P. J., and M. G. Gehring, 2000: Real-time prediction of the lake breeze on the western shore of Lake Michigan. *Wea. Forecasting*, **15**, 298–312, doi:10.1175/1520-0434(2000)015<0298:RTPOTL>2.0.CO;2.
- , D. M. Schultz, and R. Romero, 2002: Synoptic regulation of the 3 May 1999 tornado outbreak. *Wea. Forecasting*, **17**, 399–429, doi:10.1175/1520-0434(2002)017<0399:SROTM>2.0.CO;2.
- Schultz, D. M., and C. A. Doswell III, 2000: Analyzing and forecasting Rocky Mountain lee cyclogenesis often associated with strong winds. *Wea. Forecasting*, **15**, 152–173, doi:10.1175/1520-0434(2000)015<0152:AAFRML>2.0.CO;2.
- Sippel, J. A., and F. Zhang, 2008: A probabilistic analysis of the dynamics and predictability of tropical cyclogenesis. *J. Atmos. Sci.*, **65**, 3440–3459, doi:10.1175/2008JAS2597.1.
- Skamarock, W. C., and Coauthors, 2008: A description of the Advanced Research WRF version 3. NCAR Tech. Note NCAR/TN-475+STR, 113 pp. [Available online at [http://www.mmm.ucar.edu/wrf/users/docs/arw\\_v3\\_bw.pdf](http://www.mmm.ucar.edu/wrf/users/docs/arw_v3_bw.pdf).]
- Stensrud, D. J., and S. J. Weiss, 2002: Mesoscale model ensemble forecasts of the 3 May 1999 tornado outbreak. *Wea. Forecasting*, **17**, 526–543, doi:10.1175/1520-0434(2002)017<0526:MMEFOT>2.0.CO;2.
- , H. E. Brooks, and S. J. Weiss, 2003: Weather prediction: Severe weather forecasting. *Encyclopedia of the Atmospheric Sciences*, J. A. Curry and J. A. Pyle, Eds., Vol. 6, Academic Press, 2568–2576.
- Thompson, G., P. R. Field, R. M. Rasmussen, and W. D. Hall, 2008: Explicit forecasts of winter precipitation using an improved bulk microphysics scheme. Part II: Implementation of a new snow parameterization. *Mon. Wea. Rev.*, **136**, 5095–5115, doi:10.1175/2008MWR2387.1.
- Thompson, R. L., R. Edwards, J. A. Hart, K. L. Elmore, and P. Markowski, 2003: Close proximity soundings within supercell environments obtained from Rapid Update Cycle. *Wea. Forecasting*, **18**, 1243–1261, doi:10.1175/1520-0434(2003)018<1243:CPSWSE>2.0.CO;2.
- Uccellini, L. W., 2014: Service Assessment: May 2013 Oklahoma tornadoes and flash flooding. U.S. Dept. of Commerce/NOAA/NWS, Silver Spring, MD, 63 pp. [Available online at [http://www.nws.noaa.gov/os/assessments/pdfs/13oklahoma\\_tornadoes.pdf](http://www.nws.noaa.gov/os/assessments/pdfs/13oklahoma_tornadoes.pdf).]
- Wandishin, M. S., D. J. Stensrud, S. L. Mullen, and L. J. Wicker, 2008: On the predictability of mesoscale convective systems: Two-dimensional simulations. *Wea. Forecasting*, **23**, 773–785, doi:10.1175/2008WAF2007057.1.
- , —, —, and —, 2010: On the predictability of mesoscale convective systems: Three-dimensional simulations. *Mon. Wea. Rev.*, **138**, 863–885, doi:10.1175/2009MWR2961.1.
- Weisman, M. L., and J. B. Klemp, 1982: The dependence of numerically simulated convective storms on vertical wind shear and buoyancy. *Mon. Wea. Rev.*, **110**, 504–520, doi:10.1175/1520-0493(1982)110<0504:TDONSC>2.0.CO;2.
- , and —, 1984: The structure and classification of numerically simulated convective storms in directionally varying wind shears. *Mon. Wea. Rev.*, **112**, 2479–2498, doi:10.1175/1520-0493(1984)112<2479:TSACON>2.0.CO;2.
- Wu, D., Z. Meng, and D. Yan, 2013: The predictability of a squall line in South China on 23 April 2007. *Adv. Atmos. Sci.*, **30**, 485–502, doi:10.1007/s00376-012-2076-x.
- Zhang, D., and R. A. Anthes, 1982: A high-resolution model of the planetary boundary layer—Sensitivity tests and comparisons with SESAME-79 data. *J. Appl. Meteor.*, **21**, 1594–1609, doi:10.1175/1520-0450(1982)021<1594:AHRMOT>2.0.CO;2.
- Zhang, F., C. Snyder, and R. Rotunno, 2002: Mesoscale predictability of the “surprise” snowstorm of 24–25 January 2000. *Mon. Wea. Rev.*, **130**, 1617–1632, doi:10.1175/1520-0493(2002)130<1617:MPOTSS>2.0.CO;2.
- , A. M. Odins, and J. W. Nielse-Gammon, 2006: Mesoscale predictability of an extreme warm-season precipitation event. *Wea. Forecasting*, **21**, 149–166, doi:10.1175/WAF909.1.
- Zhang, Y., Z. Meng, F. Zhang, and Y. Weng, 2014: Predictability of tropical cyclone intensity evaluated through 5-yr forecasts with a convection-permitting regional-scale model in the Atlantic basin. *Wea. Forecasting*, **29**, 1003–1023, doi:10.1175/WAF-D-13-00085.1.
- Ziegler, C. L., and E. N. Rasmussen, 1998: The initiation of moist convection at the dryline: Forecasting issues from a case study perspective. *Wea. Forecasting*, **13**, 1106–1131, doi:10.1175/1520-0434(1998)013<1106:TIOMCA>2.0.CO;2.